Article

Supramolecular *cis*-"Bis(Chelation)" of $[M(CN)_6]^{3-}$ (M = Cr^{III}, Fe^{III}, Co^{III}) by Phloroglucinol (H$_3$PG)

Katarzyna Jędrzejowska [1] , Jedrzej Kobylarczyk [1,2] , Dorota Glosz [1] , Emilia Kuzniak-Glanowska [1] , Dominika Tabor [1] , Monika Srebro-Hooper [1] , Jakub J. Zakrzewski [1] , Katarzyna Dziedzic-Kocurek [3] , Tadeusz M. Muzioł [4] and Robert Podgajny [1,*]

[1] Faculty of Chemistry, Jagiellonian University in Krakow, Gronostajowa 2, 30-387 Kraków, Poland; katarzyna.jedrzejowska@doctoral.uj.edu.pl (K.J.); jedrzej.kobylarczyk@ifj.edu.pl (J.K.); doglosz@wp.pl (D.G.); kuzniak.emilia@gmail.com (E.K.-G.); dominika.tabor@student.uj.edu.pl (D.T.); monika.srebro@uj.edu.pl (M.S.-H.); jakub.j.zakrzewski@doctoral.uj.edu.pl (J.J.Z.)
[2] Institute of Nuclear Physics PAN, Radzikowskiego 152, 31-342 Kraków, Poland
[3] Marian Smoluchowski Institute of Physics, Jagiellonian University, Łojasiewicza 11, 30-348 Krakow, Poland; k.dziedzic-kocurek@uj.edu.pl
[4] Faculty of Chemistry, Nicolaus Copernicus University in Toruń, Gagarina 7, 87-100 Toruń, Poland; tmuziol@umk.pl
[*] Correspondence: robert.podgajny@uj.edu.pl; Tel.: +48-12-686-2459

Abstract: Studies on molecular co-crystal type materials are important in the design and preparation of easy-to-absorb drugs, non-centrosymmetric, and chiral crystals for optical performance, liquid crystals, or plastic phases. From a fundamental point of view, such studies also provide useful information on various supramolecular synthons and molecular ordering, including metric parameters, molecular matching, energetical hierarchy, and combinatorial potential, appealing to the rational design of functional materials through structure–properties–application schemes. Co-crystal salts involving anionic *d*-metallate coordination complexes are moderately explored (compared to the generality of co-crystals), and in this context, we present a new series of isomorphous co-crystalline salts (PPh$_4$)$_3$[M(CN)$_6$](H$_3$PG)$_2$·2MeCN (M = Cr, **1**; Fe, **2**; Co **3**; H$_3$PG = phloroglucinol, 1,3,5-trihydroxobenzene). In this study, **1**–**3** were characterized experimentally using SC XRD, Hirshfeld analysis, ESI-MS spectrometry, vibrational IR and Raman, ^{57}Fe Mössbauer, electronic absorption UV-Vis-NIR, and photoluminescence spectroscopies, and theoretically with density functional theory calculations. The two-dimensional square grid-like hydrogen-bond $\{[M(CN)_6]^{3-};(H_3PG)_2\}_\infty$ network features original $\{[M(CN)_6]^{3-};(H_3PG)_4\}$ supramolecular *cis*-bis(chelate) motifs involving: (i) two double cyclic hydrogen bond synthons M(-CN···HO-)$_2$Ar, $\{[M(CN)_6]^{3-};\mathbf{H_2}PGH\}$, between *cis*-oriented cyanido ligands of $[M(CN)_6]^{3-}$ and resorcinol-like face of H$_3$PG, and (ii) two single hydrogen bonds M-CN···HO-Ar, $\{[M(CN)_6]^{3-};\mathbf{H}PGH_2\}$, involving the remaining two cyanide ligands. The occurrence of the above tectonic motif is discussed with regard to the relevant data existing in the CCDC database, including the multisite H-bond binding of $[M(CN)_6]^{3-}$ by organic species, mononuclear coordination complexes, and polynuclear complexes. The physicochemical and computational characterization discloses notable spectral modifications under the regime of an extended hydrogen bond network.

Keywords: hydrogen bond; cyanidometallates; co-crystals; molecular tectons; molecular synthons; Hirshfeld analysis; ETS-NOCV analysis

1. Introduction

Hexacyanidometallates of *d* block metal ions belong to the most versatile and common building blocks in the construction of functional molecular materials within the frame of various synthetic strategies. Based on their individual properties resulting from the valence electronic structure (magnetic, optical, redox reactivity, communicative molecular orbital system), polynuclear complexes are considered in the construction of switchable materials

such as molecular magnets, nanomagnets, and photomagnets or solar energy converting units. These features are very often combined and enhanced with porosity, conductivity, or luminescence under the common flag of the Prussian Blue Analogues (PBAs) family and the related species of various dimensionality [1–3].

Nevertheless, going beyond the bimetallic or trimetallic building block approach toward coordination-based networks, another broad field has emerged, focusing on the development of an alternative molecular networks library. As in the case of PBAs, organic and inorganic parties in such networks meet together in shaping their properties and functionality; however, within the current scenery, the $[M(CN)_6]^{3-}$ anions (being a representant of the broader family of anions) and "non-innocent" organic molecules are combined into hybrid supramolecular architectures through dominant non-covalent interactions. Several interesting groups of hybrid networks have been developed or at least suggested, which can be classified as real salts, double salts, or co-crystal salts, including their solvated analogues [4]. Firstly, a broad family of organic–inorganic perovskites was enriched with $[A^I][B]_2[M^{III}(CN)_6]\cdot$solv ($A^+$ = alkali metal cation, B^+ = alkyl organic cation) species, in which B^+ are located within the more or less regular cavities formed by the framework of electrostatically bound A^+ and $[M(CN)_6]^{3-}$ [5–9]. The significant freedom of reorientation shown by B^+ cations together with their symmetry and dipolar moment was exploited to imply the occurrence of thermal phase transitions between ordered/disordered states. As a result, notable switchable behavior might be observed for dielectric properties, non-centrosymmetry related properties (e.g., ferro-, pyro-, and piezoelectricity, second harmonic generation and even chirality), symmetry-independent third-harmonic generation (THG), and photoluminescent performance if appropriate species are involved [9]. Alternative molecular antiperovskite architectures were realized via reverse site occupation, hosting $[Co(CN)_6]^{3-}$ anions at the cavities formed within $\{(MF_6)(H_2dabco)_3\}^{3+}$ (M = Al^{3+}, Cr^{3+}, or In^{3+}; dabco = 1,4-diazabicyclo[2.2.2]octane) and $\{(MF_6)(H_2pip)_3\}^{3+}$ (M = Al^{3+} or Cr^{3+}; pip = piperazine) frameworks [10]. Secondly, $[M(CN)_6]^{3-}$ anions were combined with the specially preprogrammed bis(amidinium) organic dications of the dedicated directional distribution of N^+-H hydrogen bond donors, which resulted in a series of tectonic networks stabilized by charge-assisted hydrogen bonds [11,12], some of them featuring reversible solvent uptake and post-crystallization structural transformations [13,14]. The underlaying crystal phases also gave rise to a series of epitaxially grown core–shell crystalline composites [15], considered molecular waveguides exploiting luminescent properties [16]. Thirdly, planar organic cations, e.g., tetrathiafulvalene (TTF) derivatives, engaged hexacyanidometallates into the switching of charge ordering and conductivity phenomena upon structural-phase transition [17,18]. Finally, selected co-crystalline type phases combining $[M(CN)_6]^{3-}$ anions and planar neutral π-acidic species, e.g., naphtalenediimide (NDI) derivatives [19] and 1,4,5,8,9,12-hexaazatriphenylenehexacarbonitrile (HAT(CN)$_6$), showed charge transfer properties [20], whereas specially preprogrammed pyrimidine derivatives [21,22] were studied from the standpoint of surface-enhanced anion binding.

The current study is dedicated to new *d*-metallate-based supramolecular synthons that might be of importance in the design of functional molecular platforms in solution and in the solid-state. As a counterpart, we selected phloroglucinol (H$_3$PG; 1,3,5-trihydroxobenzene), a triangular hydrogen bond donor widely tested in the formation of hydrogen-bonded architectures [23–39]. Its resulting functional character is well documented in the context of topological reactivity [24], combinatorial or modular synthetic strategies [25,35], molecular recognition and selective binding [31,34,39], proton disorder [26], drugs fabrication improvement [27], luminescence switching [28], switchable magnetic properties [23], chiral properties and photonic materials [36], and general molecular organization [23,29–34,37,38]. In particular, molecular recognition and selective binding of H$_3$PG and other associated resorcinol and naphthalenediol-type co-formers involved various polynuclear d-metal ions clusters serving as the molecular hosts [31,34,39–46]. However, anionic d-metallates or f-metallates were moderately represented in these studies, count-

ing some examples of pyridine–dicarboxylate complexes forming the hydrogen-bonded networks with pyridinium and polypyridinium cations [34,43,45,46].

In this paper, we present a new series of hybrid organic–inorganic isomorphous co-crystal salts (PPh$_4$)$_3$[M(CN)$_6$](H$_3$PG)$_2$·2MeCN (M = Cr, **1**; Fe, **2**; Co **3**). As a novel contribution to the field of multicomponent molecular architectures, our structural, physicochemical, and computational studies describe the original {[M(CN)$_6$]$^{3-}$;(H$_3$PG)$_4$} supramolecular *cis*-bis(chelate) motifs involving typical single M-CN···HO-Ar and double cyclic M(-CN···HO-)$_2$Ar hydrogen-bond synthons.

2. Results and Discussion

2.1. Structural Studies

Compounds **1**–**3** crystallized in the monoclinic system, space group C2/c (Table S1). The uniformity of the powder samples and the identity of the crystals examined with SC XRD were confirmed by PXRD (Figure S1, Supplementary Materials). The crystal structures consist of PPh$_4^+$ cations, hexacyanidometallate [M(CN)$_6$]$^{3-}$ anions, phloroglucinol (H$_3$PG) co-former molecules, and solvent molecules MeCN. Asymmetric units contain 1 and $\frac{1}{2}$ PPh$_4^+$, 1 H$_3$PG, $\frac{1}{2}$ [M(CN)$_6$]$^{3-}$ anion, and 1 MeCN molecule (Figure S2), and the most important bond lengths and angles are shown in Table S2. [M(CN)$_6$]$^{3-}$ and H$_3$PG form an exclusive hydrogen-bonded 2D subnetwork {[M(CN)$_6$]$^{3-}$;(H$_3$PG)$_2$}$_\infty$, which coexists with another subnetwork formed by organic cations and solvent molecules (Figure 1a,b). The {[M(CN)$_6$]$^{3-}$;(H$_3$PG)$_2$}$_\infty$ subnetwork reveals a rhombus square grid-like topology, where [M(CN)$_6$]$^{3-}$ hydrogen-bond acceptors are located in its nodes, and H$_3$PG hydrogen bond donors act as linear linkers. Each [M(CN)$_6$]$^{3-}$ anion forms four hydrogen bond contacts with four neighboring H$_3$PG molecules (Figure 1c): two double cyclic ring-type pattern $R_2^2(12)$ synthons with two H$_3$PG, {[M(CN)$_6$]$^{3-}$;**H$_2$**PGH} and two single synthons of the linear pattern *D* with the remaining two H$_3$PG molecules, {[M(CN)$_6$]$^{3-}$;**H**PGH$_2$} [47]. Importantly, the original double synthon is formed owing to structural and electronic matching between the *cis*-dicyanido fragment of the complex and resorcinol-like [48] (1,3-dihydroxobenzene) fragment of H$_3$PG, as a vivid example of the realization of the *molecular tectonics* concept [12]. The interatomic distances and the related angles within both synthons are collected in Table 1. The observed N···O and N···H separations, together with the related almost linear N···H-O angles, allow us to classify them as moderate-to-strong hydrogen-bonding interactions [49] (see also calculated interaction energies presented in the Section 2.4 below). Among the N···O and N···H distances, the shortest ones are noted in the single {[M(CN)$_6$]$^{3-}$;(**H**PGH$_2$)} synthon along with the whole **1**–**3** series, whereas those in the {[M(CN)$_6$]$^{3-}$;(**H$_2$**PGH)} synthon are slightly longer and notably diversified, which is most probably due to steric effects that might accompany the formation of such a complex motif. The double synthons are almost planar, with a ca. 10° angle between the H$_3$PG plane and the plane formed by the *cis*-dicyanido fragment of [M(CN)$_6$]$^{3-}$. The described spatial orientation of all four synthons around the central [M(CN)$_6$]$^{3-}$ within the {[M(CN)$_6$]$^{3-}$;(**H$_2$**PGH)$_2$(**H**PGH$_2$)$_2$} structural fragment shown in Figure 1c is identical to the distribution of ligands in canonical *cis* stereoisomers of bis(chelated) six-coordinate *d* metal ion complexes [ML$_2$A$_2$] (L = bidentate chelating ligands, A = monodentate ligands), and thus we suggest to describe such aggregation as *the non-covalent cis-bischelation*. Moreover, the formation of the double synthons leads to the notable deformation of the [M(CN)$_6$]$^{3-}$ complex from octahedron following the spatial demands imposed by the distribution of the -OH groups in H$_3$PG. The C2-M1-C3 and N2···M1···N3 angles in all compounds are close to 85° and 82°, respectively, notably smaller compared to other close-to-right angles; this feature resembles the standard biting angles of ca. 72–75° observed in the complexes with the flat chelating ligands (e.g., *o*-phenanthroline). Furthermore, the M1-C3-N3 angles involved in the double synthons are visibly deviated from linearity, unlike the M1-C1-N1 and M1-C2-N2 ones. The M-C and C-N bond lengths and M-C-N angles in [M(CN)$_6$]$^{3-}$, as well as all metric parameters of H$_3$PG, are in good agreement with the statistical values

observed in the CCDC database. The overall deformation of $[M(CN)_6]^{3-}$ complexes might be represented by shape measures S_{OC-6} (Table S3) using the CShM method [50].
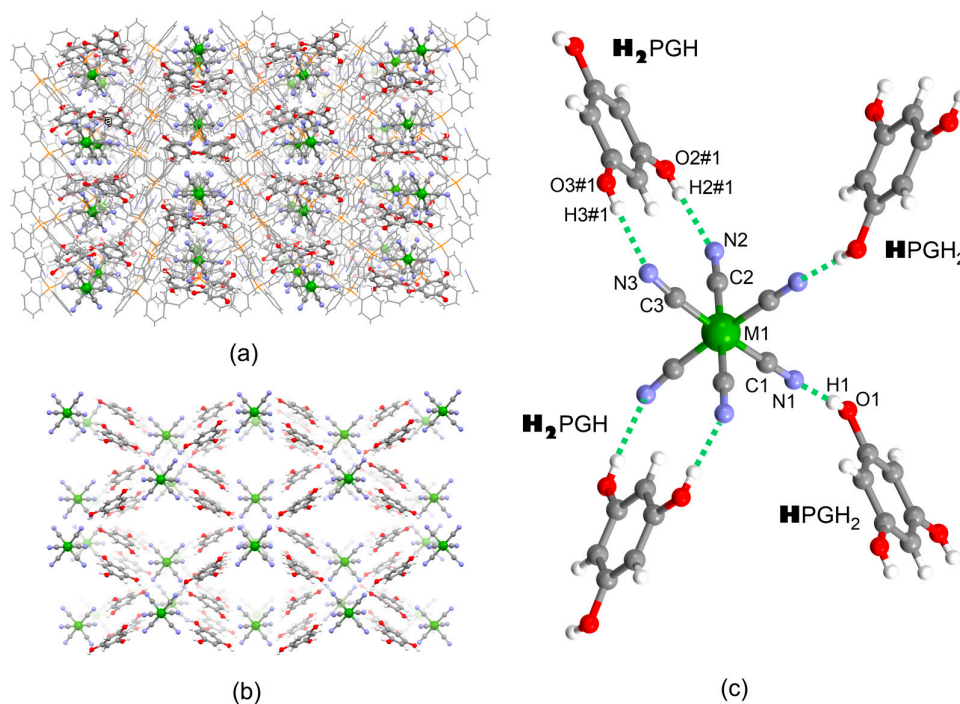
Figure 1. Crystal structure of **1–3**: (**a**) hydrogen-bonded $\{[M(CN)_6]^{3-};\{(H_3PG)_2\}$ layers spread along the *ab* crystallographic plane; (**b**) perpendicular view of hydrogen-bonded $\{[M(CN)_6]^{3-};(H_3PG)_2\}$ layers along *c* crystallographic direction (PPh$_4^+$ cations and MeCN solvent molecules omitted for clarity); (**c**) supramolecular hydrogen-bonded *cis*-"**bis(chelate)**" $\{[M(CN)_6]^{3-}(\mathbf{H_2}PGH)_2(\mathbf{H}PGH_2)_2\}$ as a part of the hydrogen-bonded single layer (for metric parameters see Table 1). Legend: green—Cr, Fe or Co, grey—C, blue—N, red—O, orange—P, white—H; protons involved in hydrogen bonds with one $[M(CN)_6]^{3-}$ are indicated in bold.

The molecular environment of the tectons engaged in the hydrogen-bond networks is completed by the oligomeric arrays of PPh$_4^+$ cations accompanied by some MeCN molecules; these components form multiple weak C-H···A interactions (A = O atoms and ring system of H$_3$PG, N atoms of $[M(CN)_6]^{3-}$) in the regions not involved in the typical hydrogen bonds (Figure S3). The $\{PPh_4^+\}_\infty$ 3D subnetwork itself provides substantial structural stabilization through so-called multiple phenyl embrace (MPE) motifs, here realized mainly by the sextuple phenyl embrace (SPE) or offset sextuple phenyl embrace (OSPE) and other hybrid patterns, with the shortest P···P distances of 6.2, 6.6, and 7.3 Å in all structures [51,52] (Figure S4).

The non-covalent *cis*-bis(chelated) $\{[M(CN)_6]^{3-}(\mathbf{H_2}PGH)_2(\mathbf{H}PGH_2)_2\}$ motif observed in the crystal structures of **1–3** obeys the local C_2 symmetry axis passing through the M1 center (this local axis converges with the lattice C_2 axes). Again, as in the case of the *cis*-bis(chelated) $[M(L_2A_2)]$ building blocks, this feature might be important from the standpoint of the molecular design of chiral and non-centrosymmetric molecular materials. Such local arrangement is a rare feature among architectures hosting non-bridged $[M(CN)_6]^{3-}$ anions and might be realized with the tris(2-aminoethyl)amine or tris(2-pyridylmethyl)amine ligand of the neighboring cationic complex [53]. On the contrary, more examples of *trans*-bischelation were found in the structural database, including synthons with multiple hydro-

gen bond donors as large cyclic alkane-polyammonium organic cations [54] or alkane-polyamine ligands of other metal complexes in the structure [55–57]. Interestingly, the hydrogen-bonded trischelation involving bis(amidinium) dications and $[M(CN)_6]^{3-}$ tectons might be distinguished along with the series of honeycomb 2D tectonic networks reported by Ferlay and Hosseini [12–14], important from the viewpoint of porosity design. However, these synthons were not considered in terms of local symmetry by these authors. Our 2D square-grid hydrogen-bonded arrangement provides a new topological solution, an alternative to the 2D honeycomb architecture based on H_3PG and $[Co_2Fe_2(CN)_6(tp^*)_2(bpy^*)_4]^{2+}$ cationic block (tp* = hydrotris(3,5-dimethylpyrazol-1-yl)borate, bpy* = 4,4′-dimethyl-2,2′-bipyridine), and involved in the thermal and light-induced electron-transfer-coupled spin transitions (ETCST) [23].

Table 1. The most important hydrogen-bonding parameters and related angles in **1**–**3** (in [Å] or in [deg]; see also Figure 1c).

Compound	1	2	3
Formula	double hydrogen bonds		
N2···O2#1 [a]	2.769	2.777	2.787
N2···H2#1	1.959	1.940	1.964
N2···H2#1-O2#1	176.89	173.77	178.21
N3···O3#1	2.815	2.827	2.835
N3···H3#1	2.016	1.987	2.056
N3···H3#1-O3#1	179.53	178.09	177.10
	related angles in $[M(CN)_6]^{3-}$		
M1-N2-C2	176.70	177.62	177.89
M1-N3-C3	171.31	173.53	173.52
C2-M1-C3	84.87	85.19	85.87
N2···M1···N3	80.82	82.01	82.75
	single hydrogen bonds		
N1···O1	2.733	2.751	2.762
N1···H1	1.944	1.916	1.949
N1···H1-O1	174.67	172.81	173.99
	related angles in $[M(CN)_6]^{3-}$		
M1-C1-N1	176.72	177.35	177.63
	88.39	89.24	89.27
C1-M1-C [b]	90.18	91.13	91.08
	91.37	91.02	91.38
	88.56	88.55	88.81
	88.37	89.14	89.19
N1···M1···N [b]	90.47	91.47	91.62
	92.26	91.89	92.06
	87.60	87.87	88.00

[a] The symmetry operation #1 is $-1/2 + x, -1/2 + y, z$. [b] Close-to-right angles involving M1-C1 bond and M1-C1-N1 angle. Compared to the C2-M1-C3 and N2···M1···N3 angles.

It must be underlined that the described hydrogen-bonded network definitely dominates the overall architecture in **1**–**3**, which results in the significant modification of the $[M(CN)_6]^{3-}$ surroundings compared to that in the crystal structures of the $(PPh_4)_3[Cr(CN)_6]\cdot 2H_2O$ (refcode SEGFAM) [58] and $(PPh_4)_3[Fe(CN)_6]\cdot 7H_2O$ (refcode VOLVEZ) [59]. This modification consists of the saturation of hydrogen-bonding connections around $[M(CN)_6]^{3-}$ exploiting much stronger Brønsted ring-OH acid compared to H-OH or ring-C-H groups (Figure S5), with a high potential to change the spectroscopic characteristics of **1**–**3** relative to their parent compounds (see below).

2.2. Hirshfeld Analysis

The square-grid-like anionic subnetwork is possible due to two synthons based on moderate-to-strong hydrogen bonds. These features can be observed on the Hirshfeld surfaces [60–62] generated for the $[Fe(CN)_6]^{3-}$ anion and H_3PG molecule (Figure 2a–d). They emerge as red spots marking distances shorter than a sum of van der Waals radii and also as spikes on corresponding fingerprints. This analysis also shows that in the case of the $[Fe(CN)_6]^{3-}$ unit, N···H interactions prevail (74.4%) (Figure S6). For H_3PG, it is only 14.7% of created contacts, but they are the shortest ones and correspond to hydrogen bonds, whereas O···H distances are more numerous (23.1%) but much longer, and the tiny spike at (1.4, 1.1) corresponds to two C-H···O hydrogen bonds (Figure S7). Both synthons can be clearly visible in Figure S8. The interface is formed by H···N and H···C atoms for double synthons and H···N for single ones. For H_3PG, the most numerous (38.2%) H···H interactions are created with surrounding PPh_4^+ cations. The C-H···N hydrogen-bonds trap PPh_4^+ units in the anionic subnetwork, which supports the compartmentalization of the cations despite electrostatic repulsion. Dance et al. explained this effect by aromatic rings embraces [51] (see above), which can also be nicely identified on Hirshfeld surfaces (Figure 2e–h). These contacts are formed by hydrogen and carbon atoms of two interacting PPh_4^+ units (Figures S9 and S10). Due to asymmetric unit content, the column pattern is given as ···P1-P1-P2··· and there are two interfaces between two P1 moieties and P1 and P2 units. Figure S11 present all interfaces involved in these interactions with prevailing H···C and H···H contacts. Mutual orientation of phenyl rings involved in this embrace points to SPE or OSPE motifs. There are also some red spots on the Hirshfeld surface which were identified as C-H···N hydrogen bonds with $[Fe(CN)_6]^{3-}$ anions and acetonitrile molecules (Figures S9g and S10g). They occur as small spikes at ca. (0.95, 1.35) and ca. (1, 1.4) (Figures S9h and S10h). Hence, these interactions are involved in the network stabilization and interactions between both sublattices (Figure 3). The positions of $(PPh_4)^+$ cations and the surface color indicate that weak interactions prevail, corresponding to X···H (X = H, C, N) created by the $[Fe(CN)_6]^{3-}$ anion and H_3PG involved in π-π interactions between strongly inclined rings.

2.3. ESI-MS

The ESI-MS spectrograms in the negative ionization mode measured for MeOH solutions of **1**–**3** do not differ significantly from each other. All of them consistently exhibit the presence of three mono-negative peak-sets assignable to the salt-like ${(PPh_4)_2[M(CN)_6]}^-$ aggregates (m/z = 886.24$^-$ for **1**, 890.23$^-$ for **2**, and 893.23$^-$ for **3**) (as a dominating feature), and to two progressive co-crystal-like ${(PPh_4)_2[M(CN)_6](H_3PG)}^-$ (m/z = 1012.27$^-$ for **1**, 1016.26$^-$ for **2**, and 1019.27$^-$ for **3**) and ${(PPh_4)_2[Fe(CN)_6](H_3PG)_2}^-$ (m/z = 1138.32$^-$ for **1**, 1142.29$^-$ for **2**, and 1145.30$^-$ for **3**) aggregates (Figures 4 and S12). A similar progression in positive ionization mode involves the mono-positive ${(PPh_4)_4[M(CN)_6]}^+$ (m/z = 1565.48$^+$ for **1**, 1569.47$^+$ for **2**, and 1572.45$^+$ for **3**) (as a dominating feature), ${(PPh_4)_4[M(CN)_6](H_3PG)}^+$ (m/z = 1691.49$^+$ for **1**, 1695.52$^+$ for **2**, and 1698.48+ for **3**), and ${(PPh_4)_4[Fe(CN)_6](H_3PG)_2}^+$ (m/z = 1821.50$^+$ observed only for **2**) aggregates (Figure S13). The absence of ${(PPh_4)_4[Cr(CN)_6](H_3PG)_2}^+$ and ${(PPh_4)_4[Co(CN)_6](H_3PG)_2}^+$ motifs might be attributed to competitive fragmentation events. Interestingly, in the spectral m/z range of 1980$^+$–2850$^+$, the Fe congener **2** shows numerous peak-sets of the isotopic patterns assignable to the aggregates of the general formula ${(PPh_4)_x[Fe(CN)_6]_y(H_3PG)_z}^{n+}$, ($x$, y, z–small natural numbers; n = 2, 3). Among them, we recognized the distinct peak-sets located at every 63 m/z unit and showed the component lines separation of m/z = 0.5 units, attributable to Fe-containing aggregates of double positive charge. The other peak-sets were located at every 42 m/z unit and exhibited the component lines separation of m/z = 0.33, and were tentatively assigned to Fe-containing aggregates of triple-positive charge. This conforms with the possible enrichment of successive aggregates with an additional H_3PG molecule (molecular mass of 126 D). The above observations indicate the notable tendency for the formation of the aggregates between $[M(CN)_6]^{3-}$ anions and H_3PG in the gas phase, which is in line with the structural data.
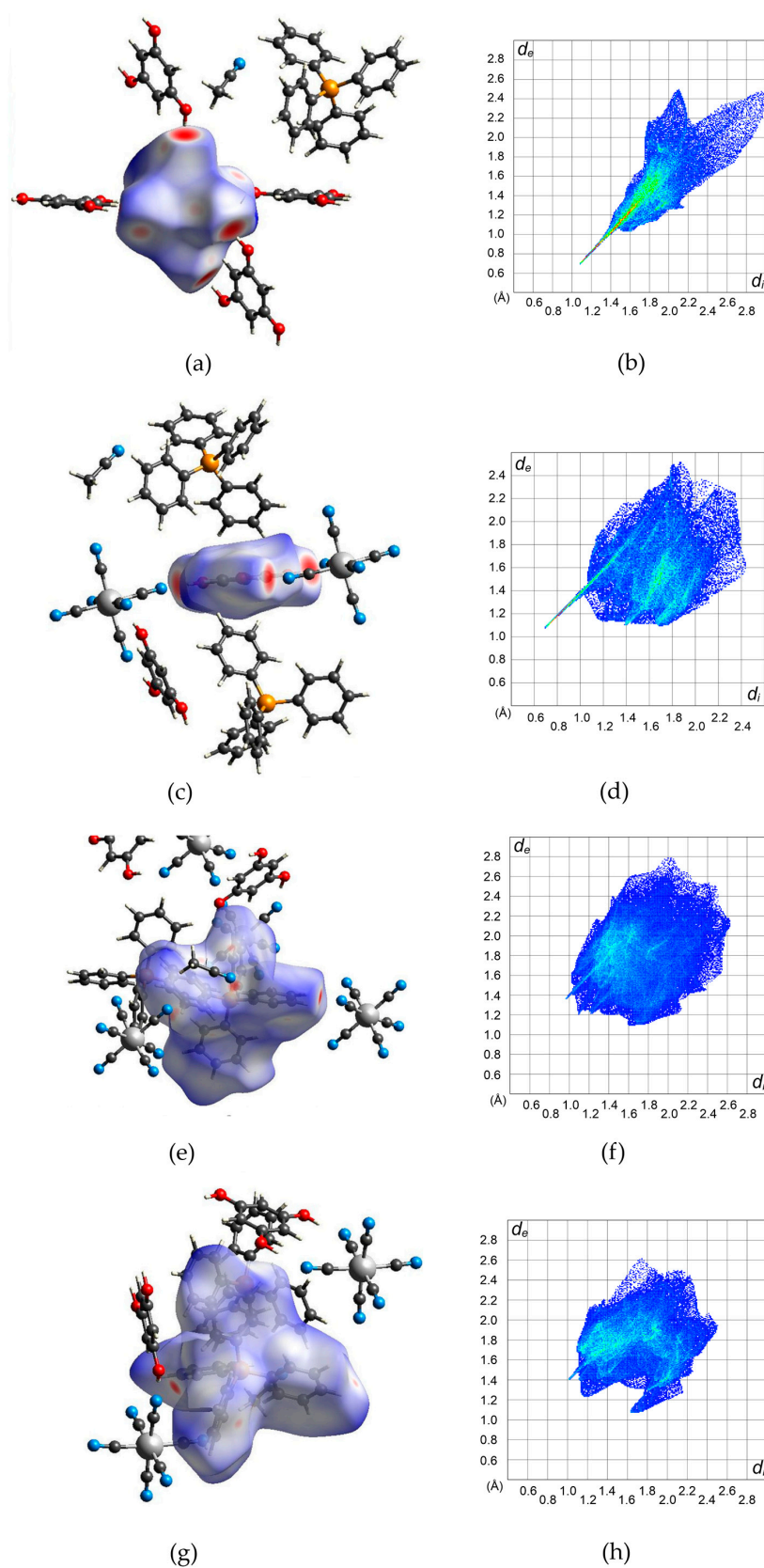
Figure 2. Hirshfeld surfaces (**left column**) of the molecular building blocks in **2** and corresponding fingerprints (**right column**) for all interactions: (**a**,**b**)–[Fe(CN)$_6$]$^{3-}$; (**c**,**d**)–H$_3$PG; (**e**,**f**)–P(1)Ph$_4^+$; (**g**,**h**)–P(2)Ph$_4^+$. The detailed images for all individual interactions are given in the Supplementary Materials (Figures S6, S7, S9 and S10).
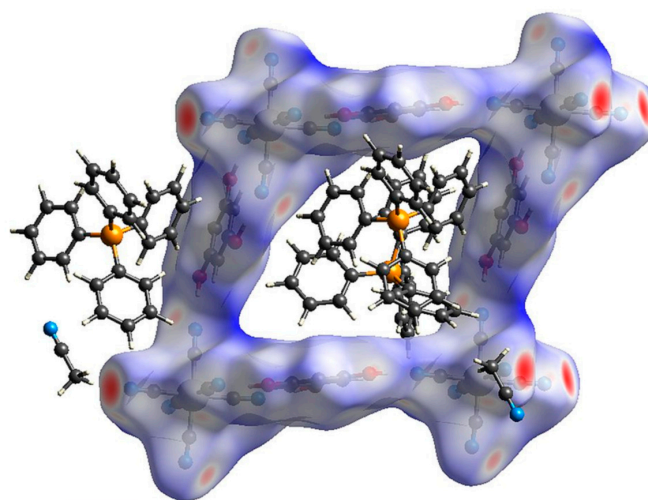
Figure 3. Hirshfeld surface presenting contacts formed by the anion subnetwork grid.

(a)

(b)
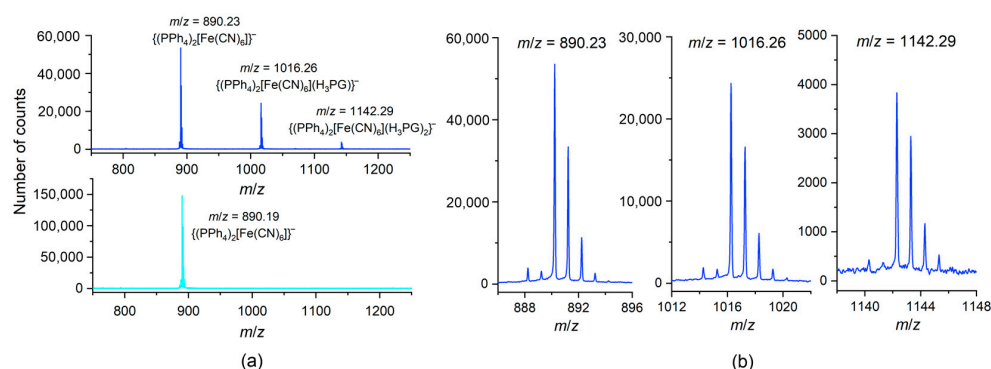
Figure 4. The ESI–MS spectra in the negative ionization mode for **2** (blue) and for $(PPh_4)_3[Fe(CN)_6] \cdot 6H_2O$ (cyan) as a reference: (**a**) the m/z range of $750^- - 1250^-$ showing the peak-sets assigned to $\{(PPh_4)_2[M(CN)_6]\}^-$, $\{(PPh_4)_2[M(CN)_6](H_3PG)\}^-$, and $\{(PPh_4)_2[Fe(CN)_6](H_3PG)_2\}^-$ aggregates; (**b**) the details of the relevant isotopic patterns. The spectra are fully representative for the whole series **1**–**3**, based on the perfect fit of the individual isotopic patterns.

2.4. DFT Calculations

To shed some light on the strength and nature of the interaction between the $[M(CN)_6]^{3-}$ anion and H_3PG molecule(s) in **1**–**3**, dispersion-corrected density functional theory (DFT + D4) [63] calculations were performed employing molecular cluster models, $\{[M(CN)_6]^{3-};$ $(\mathbf{H_2}PGH)_2(\mathbf{H}PGH_2)_2\}$, $\{[M(CN)_6]^{3-};\mathbf{H_2}PGH\}$ and $\{[M(CN)_6]^{3-};\mathbf{H}PGH_2\}$, extracted from the corresponding crystal structures. For a comparison, analogous analyses were also carried out for 4,4′-bipyridyl/H_3PG $\{4,4′bpy;\mathbf{H}PGH_2\}$ and *trans*-1,2-bis(4-pyridyl)ethylene/H_3PG $\{dpe;\mathbf{H}PGH_2\}$ clusters extracted from crystal structures reported in Refs. [25,64], respectively. A full description of computational details used in these studies, along with additional calculated results, are provided in the Supplementary Materials (Table S4, Figures S14–S17).

Tables 2 and S4 list values of interaction energy ΔE_{int} between the $[M(CN)_6]^{3-}$ and neighboring H_3PG molecule(s) (either four following the *cis*-bis(chelated) $\{[M(CN)_6]^{3-};$ $(\mathbf{H_2}PGH)_2(\mathbf{H}PGH_2)_2\}$ structural fragment or one corresponding to the double hydrogen-bonded $\{[M(CN)_6]^{3-};\mathbf{H_2}PGH\}$ and single hydrogen-bonded $\{[M(CN)_6]^{3-};\mathbf{H}PGH_2\}$ motifs) and between 4,4′bpy or dpe and H_3PG in $\{4,4′bpy;\mathbf{H}PGH_2\}$ and $\{dpe;\mathbf{H}PGH_2\}$ used as a reference. As can be seen, ΔE_{int} computed for a given motif does not show a strong dependence on the basis set nor the density functional employed in the calculations, although the double-hybrid functionals (expected to give the most accurate results [65]) systematically indicate somewhat stronger interactions between hydrogen-bond acceptor and hydrogen-bond donor molecules in the examined clusters compared to standard gradient and global

hybrid functionals. Note also that tremendously decreased magnitude interaction energies were obtained for the motifs extracted from **1–3** when the acetonitrile continuum solvent model was employed in the calculations (see Table S4), in line with additional energetic stabilization of the charged $[M(CN)_6]^{3-}$ fragment in such electrostatic medium; as in the crystal structures, the charge of the hexacyanidometallate anion is also screened to some extent by the surrounding moieties (cations in particular), and we expect the $[M(CN)_6]^{3-}/H_3PG$ interaction energies to be smaller in magnitude than those determined by the gas-phase calculations although definitely not so diminished as indicated by solvation ones. Nevertheless, all the methods uniformly demonstrate: (i) a slight increase in the magnitude of interaction energies between $[M(CN)_6]^{3-}$ and H_3PG molecule(s) in the *cis*-bis(chelated) $\{[M(CN)_6]^{3-};(H_2PGH)_2(HPGH_2)_2\}$ and double hydrogen-bonded $\{[M(CN)_6]^{3-};H_2PGH\}$ when going from system **1** (M = Cr) through **3** (Co) to **2** (Fe), (ii) overall similar values of the interaction energy between $[M(CN)_6]^{3-}$ and H_3PG in the single hydrogen-bonded $\{[M(CN)_6]^{3-};HPGH_2\}$ motif in all three compounds, and (iii) the pronounced (more than double) increase in the magnitude of these energies when compared with the corresponding single hydrogen-bonded reference clusters. We also note in passing that the computed interaction energies for $\{[M(CN)_6]^{3-};H_2PGH\}$ and $\{[M(CN)_6]^{3-};HPGH_2\}$ overall do not appear to be additive, that is, their respective sum does not reproduce (in fact, it generally exceeds) the value obtained for $\{[M(CN)_6]^{3-};(H_2PGH)_2(HPGH_2)_2\}$. This is not surprising as, in such 1:1 motifs, the H-bonding component of the $[M(CN)_6]^{3-}/H_3PG$ interaction might be more effective compared to that in the motif with $[M(CN)_6]^{3-}$ surrounded by four hydrogen-bond donor molecules. Even the interaction energy in the double $\{[M(CN)_6]^{3-};H_2PGH\}$ synthon is overall slightly smaller (less negative) than the sum of interaction energies of two simple $\{[M(CN)_6]^{3-};HPGH_2\}$ motifs. This small energetical penalty might be attributed to a minor steric hindrance that appears when two resorcinol-like H-O-ring groups accommodate the *cis*-oriented cyanido ligands in $[M(CN)_6]^{3-}$, which is in agreement with the hydrogen-bond distances observed for both motifs in the crystal structure. Nevertheless, this does not diminish the overall strength and significance of the interaction within the double cyclic synthons.
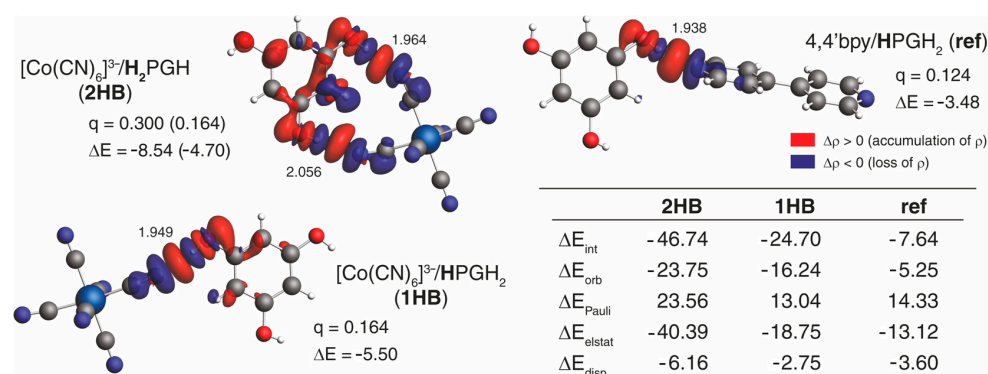
To comment on the nature of $[M(CN)_6]^{3-}/H_3PG$ interaction in **1–3**, extended transition state–natural orbitals for chemical valence (ETS-NOCV) [66] charge and bonding-energy decomposition analyses were then performed for double hydrogen-bonded $\{[Co(CN)_6]^{3-};H_2PGH\}$ and single hydrogen-bonded $\{[Co(CN)_6]^{3-};HPGH_2\}$ motifs, the results of which, along with those obtained for the reference systems, are presented in Figures 5 and S15–S17. As expected, the dominant NOCV contributions to the differential electron density, that is, the redistribution of electron density around $[Co(CN)_6]^{3-}$, 4,4'bpy or dpe and H_3PG in the considered molecular clusters, describe hydrogen-bonding interactions and clearly show its covalent nature via visible hydrogen-bond acceptor and donor charge-transfer (CT) interaction between the occupied lone-pair of nitrogen and the unoccupied σ* orbital of the O–H bond, accompanied in the case of $[Co(CN)_6]^{3-}/H_3PG$ by the participation of π-type orbitals of both moieties (see below) [66]. The orbital component of the hydrogen bonds present in $\{[Co(CN)_6]^{3-};H_2PGH\}$ and $\{[Co(CN)_6]^{3-};HPGH_2\}$ appears to be rather energetically similar with a slight enhancement as that in $\{[Co(CN)_6]^{3-};HPGH_2\}$, in line with its shortest distance. The one observed in $\{4,4'bpy;HPGH_2\}$, of comparable hydrogen-bonding separation as in $\{[Co(CN)_6]^{3-};HPGH_2\}$, demonstrates a non-negligible decrease, indicating that nitrogen in negatively charged $[M(CN)_6]^{3-}$ might be a better hydrogen-bond acceptor. The analysis of the interaction energy components obtained using the ETS energy decomposition scheme (see Figures 5 and S15–S17) enabled us to elucidate further a large difference in the interaction between $[Co(CN)_6]^{3-}$ and H_3PG and between 4,4'bpy or dpe and H_3PG in the considered molecular clusters. Namely, the results show that the strong interaction in $\{[Co(CN)_6]^{3-};H_2PGH\}$ and $\{[Co(CN)_6]^{3-};HPGH_2\}$ is determined by both electrostatic ΔE_{elstat} and orbital-interaction ΔE_{orb} components [67], with the latter being represented not only by the σ-CT hydrogen-bonding channel but primarily, as indicated by the analysis of other energetically relevant NOCV contributions, by the polarization (intra-CT) of the

π-electron system within H_3PG, enhanced likely due to ion–dipole interaction imposed by the negative charge of the $[Co(CN)_6]^{3-}$. Such electron-transfer channels in {4,4'bpy;**H**PGH$_2$} and {dpe;**H**PGH$_2$} are visibly diminished, which seems to be directly responsible for a pronounced decrease in the magnitude of the orbital-interaction contribution (even for {dpe;**H**PGH$_2$}, for which a shorter hydrogen-bond distance significantly strengthens its corresponding orbital component, see Figure S17). This decrease in ΔE_{orb} along with less stabilizing ΔE_{elstat} provides less counterbalance for the repulsive Pauli interaction and, accordingly, a significant drop in the absolute values of ΔE_{int} for {4,4'bpy;**H**PGH$_2$} and {dpe;**H**PGH$_2$} was observed.

Table 2. DFT-computed interaction energy ΔE_{int} values (in kcal mol^{-1}) between $[M(CN)_6]^{3-}$ (M = Cr, Fe, Co) anion and H_3PG molecule(s) in molecular clusters {$[M(CN)_6]^{3-}$;(**H$_2$**PGH)$_2$(**H**PGH$_2$)$_2$}, {$[M(CN)_6]^{3-}$;**H$_2$**PGH}, and {$[M(CN)_6]^{3-}$;**H**PGH$_2$} extracted from the crystal structures of **1**, **2**, and **3**. For comparison, the corresponding interaction energies between 4,4'-bipyridyl (4,4'bpy) and H_3PG in molecular cluster {4,4'bpy;**H**PGH$_2$} extracted from the crystal structure reported in Ref. [64] are listed.

	$[Cr(CN)_6]^{3-}$	$[Fe(CN)_6]^{3-}$	$[Co(CN)_6]^{3-}$	4,4'bpy
	BLYP + D4//TZP [a]			
(**H$_2$**PGH)$_2$ (**H**PGH$_2$)$_2$	−125.33	−133.58	−131.42	–
H$_2$PGH	−44.98	−48.44	−46.74	–
HPGH$_2$	†	−27.30	−24.70	−7.64
	B3LYP + D4//TZP [a]			
(**H$_2$**PGH)$_2$ (**H**PGH$_2$)$_2$	−124.87	−133.38	−130.88	–
H$_2$PGH	−44.65	−47.98	−46.40	–
HPGH$_2$	−22.30	−24.29	−23.99	−7.70
	rev-DOD-BLYP + D4//TZ2P [a]			
(**H$_2$**PGH)$_2$ (**H**PGH$_2$)$_2$	−134.00	−142.66	−138.84	–
H$_2$PGH	−47.28	−51.02	−48.77	–
HPGH$_2$	−23.99	−26.60	−26.46	−9.50

[a] The results shown were computed in a vacuum with dispersion-corrected DFT + D4 employing exchange–correlation density functionals belonging to different classes of approximation, BLYP (gradient), B3LYP (global hybrid), and rev-DOD-BLYP (double hybrids), and the indicated basis set (TZP or TZ2P). See Supplementary Materials for a full set of calculated data. † Calculations failed to reach SCF convergence for the motif.

	2HB	1HB	ref
ΔE_{int}	- 46.74	- 24.70	- 7.64
ΔE_{orb}	- 23.75	- 16.24	- 5.25
ΔE_{Pauli}	23.56	13.04	14.33
ΔE_{elstat}	- 40.39	- 18.75	- 13.12
ΔE_{disp}	- 6.16	- 2.75	- 3.60

Figure 5. Results of ETS-NOCV analysis of the interaction between $[M(CN)_6]^{3-}$ anion and H_3PG molecule in {$[Co(CN)_6]^{3-}$;**H$_2$**PGH} and {$[Co(CN)_6]^{3-}$;**H**PGH$_2$} molecular clusters extracted from the crystal structure of **3** and between 4,4'-bipyridyl (4,4'bpy) and H_3PG in {4,4'bpy;**H**PGH$_2$} molecular cluster extracted from the crystal structure reported in Ref. [64] used here as a reference. Isosurfaces (± 0.0005 au) of dominant NOCV contributions to the differential electron density $\Delta \rho$ describing hydrogen bonding along with their charge (q in e) and orbital energy (ΔE in kcal mol^{-1}) assessment.

Two values of q and ΔE provided for the {[Co(CN)$_6$]$^{3-}$;**H$_2$**PGH} motif correspond to the total assessment for both hydrogen bonds and to the shortest one only (given in parentheses). Numbers listed close to the O–H···N contacts are the hydrogen-bond distances, in Å. In the table: The corresponding interaction energy components (in kcal mol^{-1}) as obtained using the ETS energy decomposition scheme are presented. Based on BLYP + D4//TZP calculations.

2.5. Spectroscopic Studies

2.5.1. Vibrational Studies

The IR spectra of **1–3** in the 4000–700 cm^{-1} and 600–100 cm^{-1} range (Figures 6a, S18 and S19) combine the spectral features of all relevant structural components: ν(O-H) vibrations of H$_3$PG; ν(C-H) vibrations of H$_3$PG, PPh$_4^+$ and MeCN; ν(C≡N) vibrations of [M(CN)$_6$]$^{3-}$ and MeCN, and a full set of skeletal vibrations of H$_3$PG and PPh$_4^+$ (*for details see* Materials and methods). H$_3$PG and all co-crystal salts **1–3** show a significant spread of the band assigned to the ν(O-H) vibrations in the 3600–2500 cm^{-1} range due to the presence of a hydrogen-bond network. However, for **1–3,** the high wavenumber limit and the position of the band maximum are visibly shifted to lower energy (all in cm^{-1}): from 3600 to ca. 3470 and from 3195 to ca. 3120, respectively. This can be interpreted in terms of the increased strength of hydrogen bonds (and decreased strength of O-H bonds) in **1–3** compared to those in H$_3$PG [35,36,68], expected based on the difference in Brønsted acidity of H$_3$PG and H$_2$O and the basicity of H$_3$PG and [M(CN)$_6$]$^{3-}$. The bands characteristic of ν(C≡N) are notably shifted to the higher wavenumber (*ca.* 20 cm^{-1}) in **1–3** compared to the precursors (all in cm^{-1}): from 2112 m towards 2126 m, 2129 m, and 2140 m for **1**, from 2098 s, 2109 w, and 2116 vw towards 2116 s, 2129 w and 2135 vw for **2**, and from 2106 m(sh), 2109 s and 2122 towards 2128 s and 2140 m for **3** (Figure 6a) [20,69–71]. The above spectral changes are consistent with the occurrence of CN$^-$···H-O$_{H3PG}$ hydrogen bonds, notably stronger and extended, compared to rather local CN$^-$···H-O$_{H2O}$ hydrogen bonds observed in the crystal structures of (PPh$_4$)$_3$[M(CN)$_6$]·nH$_2$O salts (Figure S5) [58,59]. While the fingerprint region is not diagnostic for the modification of the vibrational (and electronic) structure (Figure S18), the spectra in the FIR region 600–100 cm^{-1} indicate notable hipsochromic shifts of the skeletal δ(Cr-C-N), δ(Cr-C-N), and ν(Cr-C) vibrations, and bathochromic shifts of selected H$_3$PG vibrations (Figure S19), being representative to the whole **1–3** series [9,69,72]. Modification of vibrational structure in **1** compared to the precursors, occurring due to a relocation of the electronic density as the result of the hydrogen-bonding architecture, was also confirmed by Raman spectra (Figures S20–S22) [69].
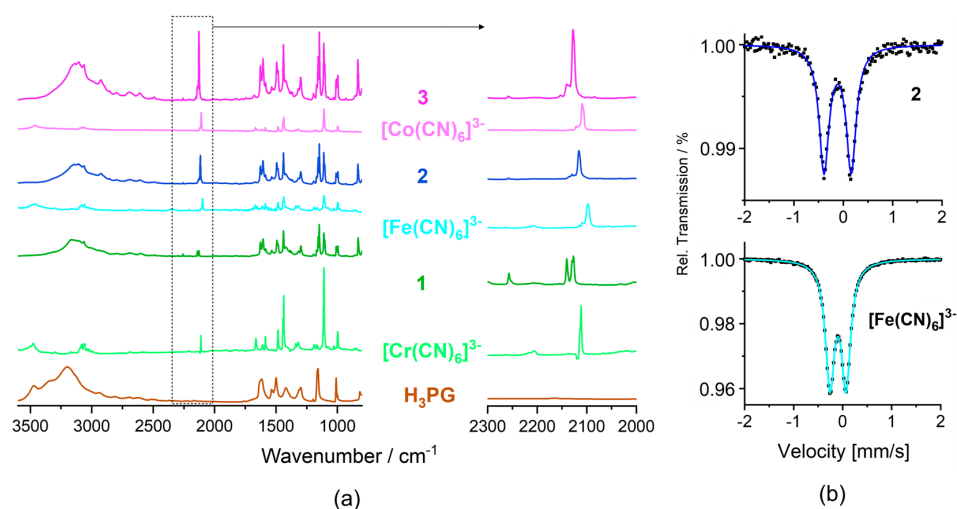
Figure 6. (**a**) Infrared spectra of **1-3** in the absorption mode compared with the spectra of H$_3$PG and (PPh$_4$)$_3$[M(CN)$_6$]·nH$_2$O precursor salts with enlargement of including the ν(C≡N) stretching vibration range shown on the right. (**b**) ^{57}Fe Mössbauer spectra of **2** (**top**) and of the (PPh$_4$)$_3$[Fe(CN)$_6$]·7H$_2$O precursor (**bottom**).

2.5.2. ^{57}Fe Mössbauer Spectra

The solid-state ^{57}Fe Mössbauer spectra for **2** and the $(PPh_4)_3[Fe(CN)_6] \cdot 7H_2O$ reference are presented in Figure 6b. Both spectra were reproduced using single doublets assignable to the low-spin (LS) Fe^{III} state expected for the LS $[Fe(CN)_6]^{3-}$ anion. Co-crystal salt **2** reveals the isomeric shift δ_2 = –0.11 mm s^{-1}, and quadrupole splitting QS$_2$ = 0.55 mm s^{-1}. δ_2 is smaller than δ_{ref} = –0.09 mm s^{-1} for the reference salt, which is in line with more significant electron density removal from the 3 d metal valence orbitals expected for more extended and stronger hydrogen bonds $_{CN}$N···H-O$_{H3PG}$ in **2** compared to those present in the reference salt. QS$_2$ is considerably larger than QS$_{ref}$ = 0.33 mm s^{-1} for the reference, which might be related to a specific distribution of the cyanido ligands of the local C$_2$ symmetry and slightly decreased degeneracy of the t$_{2g}$ orbital set due to the bis(chelate)-like arrangement of four H$_3$PG hydrogen bond donors. The observed negative correlation between δ and QS change is in line with the tendency found for a set of hydrated and dehydrated PBAs [1,73].

2.5.3. UV-Vis Electronic Absorption Spectra

The colors of the starting materials are: white for H$_3$PG, pale yellow for $[Cr(CN)_6]^{3-}$ salt, yellow for $[Fe(CN)_6]^{3-}$ salt, and white for $[Co(CN)_6]^{3-}$ salt, whereas the obtained co-crystal salts are yellow (**1**), yellow–brownish (**2**), and pale yellow (**3**). The solid-state UV-Vis absorption spectra for **1–3,** together with the spectra of H$_3$PG and of the respective $(PPh_4)_3[M(CN)_6] \cdot nH_2O$ precursors in the 200–800 nm range, are presented in Figure 7. In general, the most important spectral features characteristic for $[M(CN)_6]^{3-}$ and H$_3$PG units were reproduced for **1–3**, and below, we only discuss the directly detectable changes observed individually for each product compared to the spectra of the precursors.

Compounds **1** and **3** showed the hypsochromic shift of the bands assignable to the lowest energy spin-allowed transitions as compared to $(PPh_4)_3[Cr(CN)_6] \cdot 2H_2O$ and $(PPh_4)_3[Co(CN)_6] \cdot 6H_2O$, respectively. For **1**, the energies of the $^4A_{2g} \rightarrow {}^4T_{2g}$ (^{4}F) and $^4A_{2g} \rightarrow {}^4T_{1g}$ (^{4}F) transitions [9,69,74–77] were increased from 388 to 380 nm (ΔE = 550 cm^{-1}) and from 315 to ca. 290 nm (ΔE of at least of 2700 cm^{-1}; this estimation lacks exactness due to the bands' overlap). For **3**, the energy of the $^1A_{1g} \rightarrow {}^1T_{1g}$ transition [70,76–79] was shifted from 324 to ca. 297 nm (Δ of at least 2800 cm^{-1}). For the Fe(CN)$_6$$^{3-}$ analogue, the lowest-energy range was dominated by ligand-to-metal charge-transfer (LMCT) σ(CN$^-$) $\rightarrow$ π(2t$_{2g}$) transitions with a possible admixture of one of the ligand-field (LF) spin-forbidden transitions [71,76,77,80]. While the whole band was also shifted to a higher energy from 433 nm for the reference towards 422 nm for **2** (ΔE = 600 cm^{-1}), another feature centered at ca. 490 nm appeared for **2**, covering the range up to 750 nm. All observed changes should be interpreted in terms of the stabilization or destabilization of the relevant metal and cyano-ligand orbitals involved in the transitions due to the relocation of electronic density along the σ- and π-channels under the impact of the electrostatic field provided by the species surrounding cyanido-ligands. For **1** and **3**, the relative increase of Δ_O splitting might be directly inferred due to the stronger electrostatic field imposed by six CN$^-$···H-O$_{H3PG}$ hydrogen bonds, compared to the CN$^-$···H-O$_{water}$ hydrogen bonds observed in the crystal structures of $(PPh_4)_3[M(CN)_6] \cdot nH_2O$ salts [58,59]. The range of the Δ_O change is comparable to those reported for $[Cr(CN)_6]^{3-}$ and $[Co(CN)_6]^{3-}$ anions in the solid matrices of alkali metal halides; however, a sign of this change might depend on the distance and geometry of CN···cation motif [69,70,75]. The theoretical consideration of the energy levels for the mono-ionized $[Co(CN)_6]^{4-}$ anion suggests that our observations for **1** and **3** might be due to the relative stabilization of 2t$_{2g}$ orbitals, from where the electrons are excited in the LF states [79]. In the case of **2**, the interpretation is not so straightforward as the 2t$_{2g}$ orbitals
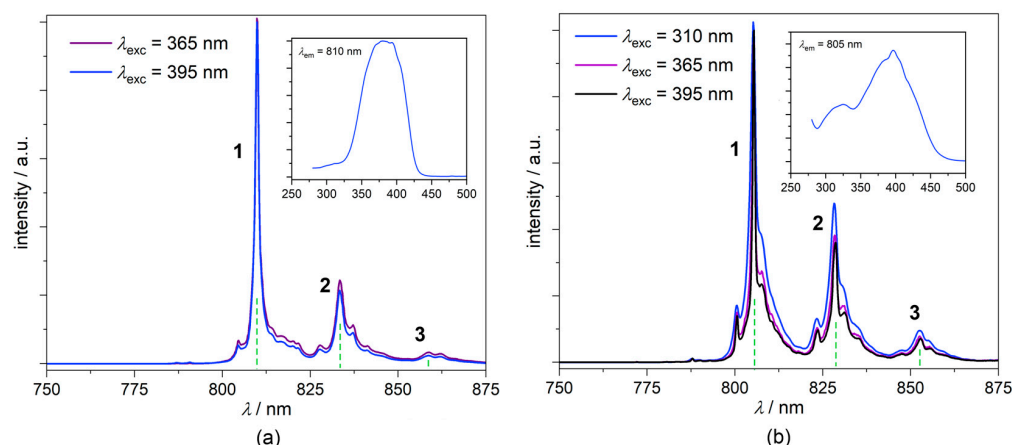
(the incomplete configuration $2t_{2g}^5$) involved in the LMCT transitions are the electron recipient levels. Thus, in this case, one should also consider the relocation of electronic density on the relevant lower energy orbitals (of $3t_{1u}$ and/or $2a_{1g}$ type) or some splitting of the involved orbitally degenerated states under the electrostatic field of hydrogen bonds [77]. The low energy spin forbidden bands of $[Cr(CN)_6]^{3-}$ and $[Co(CN)_6]^{3-}$ were scarcely detectable in our setup and were not considered in the analysis. A more precise description of the electronic structure of our co-crystal salts might be obtained with the application of more advanced experimental methods based on X-ray absorption and emission, or ultrafast photoelectron spectroscopy coupled with transient infrared studies combined with modern computational methods [71,78,80–83].

Figure 7. Electronic absorption UV-Vis spectra of **1–3** in the solid-state compared to H$_3$PG and respective (PPh$_4$)$_3$[M(CN)$_8$]·nH$_2$O precursors. The reflectance spectra were recalculated into the Kubelka-Munk finction. Colors: **1**—green, **2**—blue, and **3**—pink.

2.5.4. Photoluminescence Studies

The photoluminescence spectra of **1** and the (PPh$_4$)$_3$[Cr(CN)$_6$]·2H$_2$O reference at 77 K are presented in Figure 8, both revealing three distinguishable bands of the location and maximum lines specified in Table 3. The photoluminescence pattern observed in the range 750–875 nm is assigned to the $^2E_g \rightarrow {}^4A_{2g}$ phosphorescence characteristic of various inorganic solids and hybrid molecular solids involing $[Cr(CN)_6]^{3-}$ moiety [9,69,75,84,85] and may be interpreted in terms of its vibronic properties. The positions of these bands are usually indicated in respect to the R_1 (0'-0) emission line (here not measured, however, expected to be located at ca. 795–800 nm) and might be attributed to the specific fundamental modes involving some of the skeletal δ(C-Cr-C), δ(Cr-C-N) and δ(Cr-C) vibrations (below 450–500 cm^{-1}; ν_9, ν_{13}, ν_7, ν_8, and ν_{12} in the increasing energy order) and combination modes (above 500 cm^{-1}) [9,69,75]. The systematic bathochromic shift of ca. 5 nm was observed, going from (PPh$_4$)$_3$[Cr(CN)$_6$]·2H$_2$O to **1**, which might be interpreted in terms of the modification of molecular surroundings described above, and correlates with the hypsochromic shift of the $^4A_{2g} \rightarrow {}^4T_{2g}$ (^{4}F) and $^4A_{2g} \rightarrow {}^4T_{1g}$ (^{4}F) transitions in the UV-Vis spectra. This nicely corresponds with the systematic increase of the relevant absorption energy and decrease of the $^2E_g \rightarrow {}^4A_{2g}$ phosphorescence energy observed for the solid phases of (PPh$_4$)$_3$[Cr(CN)$_6$]·2H$_2$O, **1**, and K$_3$[Cr(CN)$_6$], coming from the first one to the last one [69,75,84]. The emission lifetimes τ_1 determined using the equation corresponding to the single decay process are (all in ms): 6.8 (77 K) and 5.5 (298 K) for (PPh$_4$)$_3$[Cr(CN)$_6$]·2H$_2$O, and 5.1 (77 K) and 4.5 (298 K) for **1** (λ_{exc} = 395 nm followed at the various accessible emission lines) (Figures S23 and S24). The observed slight decrease of τ_1 for **1** might be tentatively attributed to the specific character of hydrogen bond architecture in **1** described above. The shortening of lifetimes coincides with the decrease of average luminescence quantum yields measured at room temperature, from 10.9(2)% for (PPh$_4$)$_3$[Cr(CN)$_6$]·2H$_2$O to 8.84(4)% for **1**. More detailed information could be inferred from LHe measurements, supported by computational methods, which are beyond the scope of this study.

Figure 8. $^2E_g \rightarrow {}^4A_{2g}$ emission spectra of **1** (**a**) and $(PPh_4)_3[Cr(CN)_6]\cdot 2H_2O$ reference (**b**) at various excitation wavelengths in $T = 77$ K. The insets show the excitation spectra at λ_{em} related to the highest emission intensity in emission spectra.

Table 3. The energy of $^2E_g \rightarrow {}^4A_{2g}$ phosphorescence bands in **1** and $(PPh_4)_3[Cr(CN)_6]\cdot 2H_2O$ in 77 K, in nm (cm^{-1}).

Compound	1	$(PPh_4)_3[Cr(CN)_6]\cdot 2H_2O$
Band 1 range	802–822 (12,469–12,165)	797–817 (12,547–12,240)
Band 1 max.	810 (12,346)	805 (12,422)
Band 2 range	825–850 (12,121–11,765)	820–842 (12,195–11,876)
Band 2 max.	833 (12,005)	828.5 (12,070)
Band 3 range	855–875 (11,696–11,428)	844–868 (11,848–11,521)
Band 3 max.	858 (11,655)	852.5 (11,730)

3. Conclusions and Perspectives

The PPh_4^+ cation-assisted supramolecular self-assembly between the $[M(CN)_6]^{3-}$ and triple-point H_3PG hydrogen bond donor led to the formation of the new 2D hydrogen-bonded network $\{[M(CN)_6]^{3-};(H_3PG)_2\}$ of square-like topology alternative to the 2D hexagonal networks formed between H_3PG and $[Co_2Fe_2(CN)_6(tp^*)_2(bpy^*)_4]^{2+}$ [23] or between $[M(CN)_6]^{3-}$ and bisaminidnium dications [13]. $[M(CN)_6]^{3-}$ complexes located in the nodes of this network are surrounded by four H_3PG molecules that form two single M-CN···HO-Ar and two double cyclic $M(-CN···HO-)_2Ar$ synthons into an original non-covalent *cis*-bis(chelated) $\{[M(CN)_6]^{3-};(H_2PGH)_2(HPGH_2)_2\}$ motif, recognized by analogy with the *cis*-bis(chelated) 6-coordinate $[ML_2A_2]$ complexes. Hirshfeld analysis indicated the notable intensity of the underlaying interactions. The strong mutual affinity of both tectons was confirmed by ESI-MS spectrometry and was nicely quantified by the substantial energies of interactions reaching ca. 23–27 kcal mol^{-1} for simple $\{[M(CN)_6]^{3-};HPGH_2\}$ and ca. 45–50 kcal mol^{-1} for double cyclic $\{[M(CN)_6]^{3-};H_2PGH\}$ motifs obtained based on the gas-phase DFT + D4 calculations for the molecular clusters extracted from the crystal structures. Thus, the H_3PG proved to be an efficient double-point receptor unit for $[M(CN)_6]^{3-}$ anions thanks to the molecular matching between the resorcinol-like face of H_3PG and *cis*-oriented pairs of cyanido ligands of $[M(CN)_6]^{3-}$. The observed $\{[M(CN)_6]^{3-};(H_2PGH)_2(HPGH_2)_2\}$ motif revealed chiral (C_2) local surroundings of the $[M(CN)_6]^{3-}$ complex, which might be of importance in the broader context of supramolecular design towards interesting symmetry-related structure-properties schemes. The spectroscopic characteristics of **1–3** revealed notable modifications as compared to the $(PPh_4)_3[M(CN)_6]\cdot nH_2O$ references characterized by less saturated hydrogen-bond surroundings of $[M(CN)_6]^{3-}$ involving relatively weaker hydrogen-bond donors; this also includes the photoluminescent properties of the $[Cr(CN)_6]^{3-}$ anion.

The above findings might be important from the standpoint of the design of modular multisite anion receptors dedicated to binding of d-metallates and the development of alternative pathways towards the controlled synthesis of new multicomponent (coordination-based, hybrid organic-inorganic, etc.) architectures and materials of functional features. In particular, the targeted CCDC search indicates the existence of several very interesting complex molecular motifs exhibiting multiple resorcinol groups [86–93]; they may be definitely considered as potential platforms for multisite anions receptors exploiting the synthons described in this manuscript. Advanced research in this direction is underway in our group.

4. Materials and Methods

$K_3[Fe(CN)_6]$, $K_3[Co(CN)_6]$, $K_3[Cr(CN)_6]$, PPh_4Cl, PPh_4Br, 1,3,5-trihydroxybenzene, and solvents were purchased from a commercial source (Sigma-Aldrich, Alfa Aesar, etc.) and used without further purification.

4.1. Synthetic Procedures

$(PPh_4)_3[Fe(CN)_6]\cdot7H_2O$, $(PPh_4)_3[Co(CN)_6]\cdot6H_2O$, and $(PPh_4)_3[Cr(CN)_6]\cdot2H_2O$ were prepared by metathesis of the corresponding potassium salts of the complexes with PPh_4Cl.

Synthesis of 1. Acetonitrile solutions of $(PPh_4)_3[Cr(CN)_6]\cdot2H_2O$ (0.227 g, 0.18 mmol in 15 mL of CH_3CN) and H_3PG (0.0324 g, 0.2 mmol in 15 mL of CH_3CN) were mixed to obtain a colorless solution, and the mixture was tightly closed in the vessel. After one day, pale yellow crystals of **1** appeared. The crystals were filtered and washed with cold acetonitrile (10 mL, 2 °C) and dried in air. The composition of $(PPh_4)_3[Cr(CN)_6](H_3PG)_2\cdot2MeCN$ was defined by a single-crystal X-ray diffraction analysis. Phase purity was proved by XRD data. Yield: 0.168 g, 60.0%. Elemental analysis. Calc. for $C_{94}H_{78}CrN_8O_6P_3$ (Mw = 1560.55 g·mol^{-1}): C, 72.34%; H, 5.04%; N, 7.18%. Found: C, 72.1%; H, 5.0%; N, 7.1%. IR (KBr, cm^{-1}): 3470–2500 v(O-H), 3059 v(C-H), 2257 v(C≡N) (MeCN), 2126, 2129, 2140 v(C≡N) ($[Cr(CN)_6]^{3-}$), other: 1585, 1481, 1438, 1186, 1109, and 995 (vibrations of PPh_4^+) 1626, 1606, 1491, 1419 br, 1297, 1155,1146, 1010, 1004, and 832 (vibrations of H_3PG). Solubility: MeOH–good, CH_3CN–poor. Stability: composition stable up to ca. 80 °C, then loses 2 crystallization MeCN molecules in the range 80–140 °C; above 190 °C massive decomposition occurs (Figure S25).

Synthesis of 2. Acetonitrile solutions of $(PPh_4)_3[Fe(CN)_6]\cdot6H_2O$ (0.240 g, 0.018 mmol in 15 mL of CH_3CN) and H_3PG (0.0324 g, 0.2 mmol in 15 mL of CH_3CN) were mixed to obtain a pale yellow solution, and the mixture was tightly closed in the vessel. After one day, brown–yellow crystals of **2** appeared. The crystals were filtered and washed with cold acetonitrile (10 mL, 2 °C) and dried in air. The composition of $(PPh_4)_3[Fe(CN)_6](H_3PG)_2\cdot2MeCN$ was defined by a single-crystal X-ray diffraction analysis. Phase purity was proved by XRD data. Yield: 0.180 g, 64.0%. Elemental analysis. Calc. for $C_{94}H_{78}FeN_8O_6P_3$ (Mw = 1564.40 g·mol^{-1}): C, 72.17%; H, 5.03%; N, 7.16%. Found: C, 72.2%; H, 5.0%; N, 7.2%. IR (KBr, cm^{-1}): 3445–2500 v(O-H), 3063 v(C-H), 2257 v(C≡N) (MeCN), 2116, 2130, 1441 v(C≡N) ($[Fe(CN)_6]^{3-}$); other: 1585, 1481, 1438, 1186, 1109, and 995 (vibrations of PPh_4^+) 1626, 1606, 1491, 1419 br, 1297, 1155,1146, 1010, 1004, 832 (vibrations of H_3PG). Solubility: MeOH–good, CH_3CN–poor. Stability: composition stable up to ca. 70 °C, then loses 2 crystallization MeCN molecules in the range 70–130 °C; above 170 °C massive decomposition occurs (Figure S25).

Synthesis of 3. Acetonitrile solutions of $(PPh_4)_3[Co(CN)_6]\cdot7H_2O$ (0.244 g, 0.018 mmol in 15 mL of CH_3CN) and H_3PG (0.0324 g, 0.2 mmol in 15 mL of CH_3CN) were mixed to obtain a colorless solution immediately, and the mixture was tightly closed in the vessel. After one day, colorless crystals of **3** appeared. The crystals were filtered and washed with cold acetonitrile (10 mL, 2 °C) and dried in air. The composition of $(PPh_4)_3[Co(CN)_6](H_3PG)_2\cdot2MeCN$ was defined by a single-crystal X-ray diffraction analysis. Phase purity was proved by XRD data. Yield: 0.126 mg, 44.8%. Elemental analysis. Calc. for $C_{94}H_{78}CoN_8O_6P_3$ (Mw = 1567.48 g·mol^{-1}): C, 72.02%; H, 5.02%; N, 7.15%. Found: C, 72.12%; H, 4.9%; N,

7.1%. IR (KBr, cm^{-1}): 3460–2500 v(O-H), 3066 v(C-H), 2257 v(C≡N) (MeCN), 2128, 2140 v(C≡N) ([Co(CN)$_6$]$^{3+}$), other: 1585, 1481, 1438, 1186, 1109, 995 (vibrations of PPh$_4$$^+$) 1626, 1606, 1491, 1419 br, 1297, 1155,1146, 1010, 1004, 832 (vibrations of H$_3$PG). Solubility: MeOH–good, CH$_3$CN–poor. Stability: composition stable up to ca. 70 °C, then loses 2 crystallization MeCN molecules in the range 70–120 °C; above 230 °C massive decomposition occurs (Figure S25).

4.2. X-ray Diffraction Analysis

Single crystal X-ray diffraction data for all compounds were collected using a Bruker D8 Quest Eco diffractometer equipped with a Photon II detector and a Mo Kα (λ = 0.71073 Å) radiation source with a graphite monochromator and Oxford Cryostream cooling system. Crystals for measurement were taken from the mother solution and covered by NVH immersion oil. All measurements were performed in 100.0 K. Data reduction and cell parameter refinement were performed using Apex software with included SAINT and SADABS programs. Intensities of reflections for the sample absorption were corrected using the multiscan method. Structures were solved by the intrinsic phasing method and refined anisotropically with weighted full-matrix least-squares on F^2 using SHELXT [94] and SHELXL [95] programs with Olex 2 graphic interface [96].

Hydrogen atoms within structures were placed in idealized positions and refined using a riding coordinate model with isotropic displacement parameter set at 1.2–1.5 times U$_{eq}$ of appropriate carrier atoms. Crystal data and structure refinement parameters are summarized in Table S1. The structural figures in the article were prepared using the latest Mercury software [97]. The crystal structures are deposited in the CCDC database. The deposition numbers are 2,175,600 (**1**), 2,175,601 (**2**), and 2,175,602 (**3**).

4.3. Physical Techniques and Calculations

Elemental analyses of CHNS were performed on the air-dried samples using the Elemental Vario Micro Cube CHNS analyzer. Powder X-ray diffraction patterns for **1**, **2**, and **3** in 0.5 mm glass capillary were collected on a D8 Advance Eco (Bruker) using a Cu−Kα radiation source. The thermogravimetric (TGA) curves for the polycrystalline samples were collected using TG209 F1 Libra thermogravimetric analyzer with aluminum pans as holders. The data were collected in the temperature range of 21–400 °C under a nitrogen atmosphere with a heating rate of 1 °C per minute. Infrared (IR) absorption spectra in the range 4000–675 cm^{-1} were measured on the selected single-crystals using a Nicolet iN10 MX Fourier transform infrared microscope. Far infrared (FIR) spectra in the range 600–100 cm^{-1} were measured on the powder samples dispersed Apiezon N grease using an FT-IR Bruker Vertex 70 V spectrometer. Raman spectra in the range 3200–100 cm^{-1} were recorded on the microcrystalline samples with a Renishaw inVia Raman spectrometer with the excitation line 514.5 nm of Ar laser. The transmission ^{57}Fe Mössbauer spectra were collected in 1024 channels, with a 10 mCi ^{57}Co source in an Rh matrix, at room temperature using a Wissel spectrometer. The velocity scale was calibrated using the α-Fe foil standard. The powder sample was directly placed in copper rings and sealed with Kapton foil. The background spectra of the sample holders did not reveal any significant contribution to the main spectra. Mössbauer spectra were fitted with the use of the WinNormos-for-Igor software package, assuming the Lorentzian shape of the resonance lines, i.e., the saturation effects were not included. For each compound, one quadrupole doublet was considered in the fitted model, assigned to the Fe^{III} (LS) electron state. Diffuse reflectance spectra in the UV-Vis-NIR range were performed for the ground powder samples mixed with BaSO$_4$ (2 mass %) using a Shimadzu UV-3600i Plus spectrophotometer equipped with the 50 mm integrating sphere. The spectra were recalculated according to the Kubelka–Munk equation. Solid-state photoluminescent characterization for all reported compounds was performed using an FS5 spectrofluorometer (Edinburgh Instruments) equipped with a Xe arc lamp (150 W, excitation spectra) or a 365 nm diode flashlight (10 W, emission spectra) serving as excitation sources, and a Hamamatsu photomultiplier of the R928P type as a

detector. All lifetime measurements were conducted using the same spectrofluorometer employing a multichannel scaling module with a microsecond Xe flashlamp (5 W), while the collected data curves were fitted using a monoexponential decay function within a Fluoracle software (Edinburgh Instruments). Absolute quantum yields (QYs) were measured by a direct excitation method using the Xe arc lamp, an integrating sphere module (SC-30), and a Teflon pin as a reference, while the related calculations were performed within the implemented software. The Fluoracle program was also employed for the background corrections and a smoothing procedure, while for the data collected using the 365 nm flashlight, the application of a non-linear baseline was determined using the Asymmetric Least-Square Smoothing method (OriginPro 2021b) was found necessary.

4.4. Hirshfeld Analysis

The structural interaction analyses based on Hirshfeld surfaces were performed in CrystalExplorer [60–62].

4.5. Quantum-Chemical Calculations and Analyses

All computations were performed at the density functional theory (DFT) level employing molecular cluster models extracted from the corresponding crystal structures. A full description of computational details used in these studies is provided in the Supplementary Materials [63,66,98–109].

Supplementary Materials: The following supporting information can be downloaded at https://www.mdpi.com/article/10.3390/molecules27134111/s1: additional data for structural description (Figures S1–S5, Tables S1–S3); details of Hirshfeld analysis (Figures S6–S11); additional ESI-MS spectra (Figures S12 and S13); computational methodology description and additional calculated results for molecular clusters in the gas phase, and in continuum solvent model (Figures S14–S17, Table S4); additional IR spectra (fingerprint and FIR region) (Figures S18 and S19); Raman spectra (Figures S20–S22); additional emission spectra and emission lifetimes (Figures S23 and S24); TGA characteristics (Figure S25); related literature citations.

Author Contributions: K.J.: investigation—syntheses, measurements, data analysis and visualization of PXRD, TGA, IR spectroscopy, and UV-Vis electronic absorption spectroscopy, writing—original draft fragments preparation; J.K.: investigations—SC XRD structural measurements, crystal structure solution and refinement, data curation; D.G.: investigation–preliminary synthesis, structural data curation and description, participation in photoluminescence measurements, writing—original draft fragments preparation, review; E.K.-G.: participation in conceptualization, preliminary synthesis and investigation, writing—review; D.T.: investigation—DFT calculations, data analysis and visualization; M.S.-H.: conceptualization and investigation—DFT calculations, data analysis and visualization, writing—original draft fragments preparation, review; J.J.Z. investigation—photoluminescence measurements and data visualization, writing—review; K.D.-K.: investigation—measurements of ^{57}Fe Mössbauer spectra, data visualization, writing—review; T.M.M.: investigation—Hirshfeld analysis, data visualization, writing—original draft fragments preparation, review; R.P.: funding acquisition, project administration, conceptualization, supervision, writing—original draft preparation, writing—review, corresponding author. All authors have read and agreed to the published version of the manuscript.

Institutional Review Board Statement: Not applicable.

Informed Consent Statement: Not applicable.

Data Availability Statement: The insight into detailed data might be obtained after the contact with the corresponding author.

Conflicts of Interest: The authors declare no conflict of interest. The funders had no role in the design of the study; in the collection, analyses, or interpretation of data; in the writing of the manuscript, or in the decision to publish the results.

Sample Availability: Samples of compounds **1**–**3** are available from the authors.

References

1.　Avilaa, Y.; Acevedo-Peña, P.; Reguera, L.; Reguera, E. Recent progress in transition metal hexacyanometallates: From structure to properties and functionality. *Coord. Chem. Rev.* **2022**, *453*, 214274. [CrossRef]

2.　Zakrzewski, J.J.; Liberka, M.; Zychowicz, M.; Chorazy, S. Diverse physical functionalities of rare-earth hexacyanidometallate frameworks and their molecular analogues. *Inorg. Chem. Front.* **2021**, *8*, 452–483. [CrossRef]

3.　Chorazy, S.; Zakrzewski, J.J.; Magott, M.; Korzeniak, T.; Nowicka, B.; Pinkowicz, D.; Podgajny, R.; Sieklucka, B. Octacyanidometallates for multifunctional molecule-based materials. *Chem. Soc. Rev.* **2020**, *49*, 5945–6001. [CrossRef] [PubMed]

4.　Grothe, E.; Meekes, H.; Vlieg, E.; Ter Horst, J.H.; de Gelder, R. Solvates, salts, and cocrystals: A proposal for a feasible classification system. *Cryst. Growth Des.* **2016**, *16*, 3237–3243. [CrossRef]

5.　Zhang, W.; Ye, H.-Y.; Graf, R.; Spiess, H.W.; Yao, Y.-F.; Zhu, R.-Q.; Xiong, R.-G. Tunable and Switchable Dielectric Constant in an Amphidynamic Crystal. *J. Am. Chem. Soc.* **2013**, *135*, 5230–5233. [CrossRef]

6.　Qian, K.; Shao, F.; Yan, Z.; Pang, J.; Chen, X.; Yang, C. A perovskite-type cage compound as a temperature-triggered dielectric switchable material. *CrystEngComm* **2016**, *18*, 7671–7674. [CrossRef]

7.　Rok, M.; Moskwa, M.; Działowa, M.; Bieńko, A.; Rajnák, C.; Boča, R.; Bator, G. Multifunctional materials based on the double-perovskite organic—Inorganic hybrid $(CH_3NH_3)_2[KCr(CN)_6]$ showing switchable dielectric, magnetic, and semiconducting behaviour. *Dalton Trans.* **2019**, *48*, 16650–16660. [CrossRef]

8.　Rok, M.; Bator, G.; Medycki, W.; Zamponi, M.; Balčiūnas, S.; Šimėnas, M.; Banys, J. Reorientational dynamics of organic cations in perovskite-like coordination polymers. *Dalton Trans.* **2018**, *47*, 17329–17341. [CrossRef]

9.　Mączka, M.; Nowok, A.; Zaręba, J.K.; Stefańska, D.; Gągor, A.; Trzebiatowska, M.; Sieradzki, A. Near-Infrared Phosphorescent Hybrid Organic—Inorganic Perovskite with High-Contrast Dielectric and Third-Order Nonlinear Optical Switching Functionalities. *ACS Appl. Mater. Interfaces* **2022**, *14*, 1460–1471. [CrossRef]

10.　Shi, C.; Yu, H.; Wang, Q.-W.; Ye, L.; Gong, Z.-X.; Ma, J.-J.; Jiang, J.-Y.; Hua, M.-M.; Shuai, C.; Zhang, Y.; et al. Hybrid Organic–Inorganic Antiperovskites. *Angew. Chem. Int. Ed.* **2020**, *59*, 167–171. [CrossRef]

11.　Ferlay, S.; Félix, O.; Hosseini, M.W.; Planeix, J.-M.; Kyritsakas, N. Second sphere supramolecular chirality: Racemic hybrid H-bonded 2-D molecular networks. *Chem. Commun.* **2002**, 702–703. [CrossRef] [PubMed]

12.　Dechambenoit, P.; Ferlay, S.; Hosseini, M.W.; Planeix, J.-M.; Kyritsakas, N. Molecular tectonics: Control of packing of hybrid 1-D and 2-D H-bonded molecular networks formed between bisamidinium dication and cyanometallate anions. *New J. Chem.* **2006**, *30*, 1403–1410. [CrossRef]

13.　Dechambenoit, P.; Ferlay, S.; Kyritsakas, N.; Hosseini, M.W. Molecular Tectonics: Control of Reversible Water Release in Porous Charge-Assisted H-Bonded Networks. *J. Am. Chem. Soc.* **2008**, *130*, 17106–17113. [CrossRef] [PubMed]

14.　Dechambenoit, P.; Ferlay, S.; Kyritsakas, N.; Hosseini, M.W. In situ reduction of Fe(III) into Fe(II): An example of post-crystallisation transformation. *Chem. Commun.* **2009**, 6798–6800. [CrossRef]

15.　Olmsted, B.K.; Ferlay, S.; Dechambenoit, P.; Hosseini, M.W.; Ward, M.D. Microscopic Topography of Heterocrystal Interfaces. *Cryst. Growth Des.* **2009**, *9*, 2841–2847. [CrossRef]

16.　Catalano, L.; Berthaud, J.; Dushaq, G.; Karothu, D.P.; Rezgui, R.; Rasras, M.; Ferlay, S.; Hosseini, M.W.; Naumov, P. Sequencing and Welding of Molecular Single-Crystal Optical Waveguides. *Adv. Funct. Mater.* **2020**, *30*, 2003443. [CrossRef]

17.　Ota, A.; Ouahab, L.; Golhen, S.; Yoshida, Y.; Maesato, M.; Saito, G.; Świetlik, R. Phase Transition from Mott Insulating Phase into the Charge Ordering Phase with Molecular Deformation in Charge-Transfer Salts κ-(ET)$_4$[M(CN)$_6$][N(C$_2$H$_5$)$_4$]·2H$_2$O (M = Co^{III} and Fe^{III}). *Chem. Mater.* **2007**, *19*, 2455–2462. [CrossRef]

18.　Łapiński, A.; Świetlik, R.; Ouahab, L.; Golhen, S. Spectroscopic Studies of the Phase Transition from the Mott Insulator State to the Charge-Ordering State of κ-(ET)$_4$[M(CN)$_6$][N(C$_2$H$_5$)$_4$]·2H$_2$O (M = Co^{III} and Fe^{III}) Salts. *J. Phys. Chem. A* **2013**, *117*, 5241–5250. [CrossRef]

19.　You, M.-H.; Li, M.-H.; Liu, Y.-F.; Li, H.-H.; Lin, M.-J. Unprecedented five-fold interpenetrated donor–acceptor hybrid heterostructure induced by anion–π interactions. *CrystEngComm* **2019**, *21*, 6688–6692. [CrossRef]

20.　Kobylarczyk, J.; Pinkowicz, D.; Srebro-Hooper, M.; Hooper, J.; Podgajny, R. Anion–π recognition between [M(CN)$_6$]$^{3-}$ complexes and HAT(CN)$_6$: Structural matching and electronic charge density modification. *Dalton Trans.* **2017**, *46*, 3482–3491. [CrossRef]

21. Arranz-Mascarós, P.; Bazzicalupi, C.; Bianchi, A.; Giorgi, C.; Godino-Salido, M.-L.; Gutiérrez-Valero, M.-D.; Lopez-Garzón, R.; Savastano, M. Thermodynamics of Anion−π Interactions in Aqueous Solution. *J. Am. Chem. Soc.* **2013**, *135*, 102–105. [CrossRef] [PubMed]

22. Savastano, M.; Arranz-Mascarós, P.; Bazzicalupi, C.; Bianchi, A.; Giorgi, C.; Godino-Salido, M.L.; Gutiérrez-Valero, M.D.; López-Garzón, R. Binding and removal of octahedral, tetrahedral, square planar and linear anions in water by means of activated carbon functionalized with a pyrimidine-based anion receptor. *RSC Adv.* **2014**, *4*, 58505–58513. [CrossRef]

23. Sekine, Y.; Nihei, M.; Oshio, H. Dimensionally Controlled Assembly of an External Stimuli-Responsive [Co₂Fe₂] Complex into Supramolecular Hydrogen-Bonded Networks. *Chem. Eur. J.* **2017**, *23*, 5193–5197. [CrossRef] [PubMed]

24. Santra, R.; Biradha, K. Solid state double [2 + 2] photochemical reactions in the co-crystal forms of 1,5-bis(4-pyridyl)-1,4-pentadiene-3-one: Establishing mechanism using single crystal X-ray, UV and ^{1}H NMR. *CrystEngComm* **2011**, *13*, 3246–3257. [CrossRef]

25. Dubey, R.; Desiraju, G.R. Combinatorial Crystal Synthesis: Structural Landscape of Phloroglucinol:1,2-bis(4-pyridyl)ethylene and Phloroglucinol:Phenazine. *Angew. Chem. Int. Ed.* **2014**, *53*, 13178–13182. [CrossRef]

26. Thomas, L.H.; Craig, G.A.; Morrison, C.A.; Reilly, A.M.; Wilson, C.C. New Route to Local Order Models for Disordered Crystalline Materials: Diffuse Scattering and Computational Modeling of Phloroglucinol Dihydrate. *Cryst. Growth Des.* **2011**, *11*, 2045–2049. [CrossRef]

27. Guo, C.; Zhang, Q.; Zhu, B.; Zhang, Z.; Ma, X.; Dai, W.; Gong, X.; Ren, G.; Mei, X. Drug–Drug Cocrystals Provide Significant Improvements of Drug Properties in Treatment with Progesterone. *Cryst. Growth Des.* **2020**, *20*, 3053–3063. [CrossRef]

28. Pal Singh, M.; Baruah, J.B. Detection of hydroxyaromatics in a superior manner by a water soluble fluorescent iron-complex. *Inorg. Chim. Acta* **2020**, *504*, 119467. [CrossRef]

29. Sarma, B.; Sreenivas Reddy, L.; Nangia, A. The Role of π-Stacking in the Composition of Phloroglucinol and Phenazine Cocrystals. *Cryst Growth Des.* **2008**, *8*, 4546–4552. [CrossRef]

30. Braun, D.E.; Tocher, D.A.; Price, S.L.; Griesser, U.J. The Complexity of Hydration of Phloroglucinol: A Comprehensive Structural and Thermodynamic Characterization. *J. Phys. Chem. B* **2012**, *116*, 3961–3972. [CrossRef]

31. Shanmugaraju, S.; Bar, A.K.; Mukherjee, P.S. Ruthenium−Oxygen Coordination-Driven Self-Assembly of a Ru^{II}₈ Incomplete Prism: Synthesis, Structure, and Shape-Selective Molecular Recognition Study. *Inorg. Chem.* **2010**, *49*, 10235–10237. [CrossRef] [PubMed]

32. Shin, D.M.; Lee, I.S.; Chung, Y.K. Crystal Engineering with Structurally Flexible 1,1′-Substituted Ferrocenes for Nonlinear Optical Materials. *Eur. J. Inorg. Chem.* **2003**, *2003*, 2311–2317. [CrossRef]

33. Arora, K.K.; Talwelkar, M.S.; Pedireddi, V.R. Supramolecular synthesis of some molecular adducts of 4,4′-bipyridine N,N′-dioxide. *New J. Chem.* **2009**, *33*, 57–63. [CrossRef]

34. Shankar, K.; Singh, M.P.; Baruah, J.B. Extent of protonation of 4,4′-bipyridinium cations and nature of host influences the amount of guest intake by cobalt(II) 2,6-pyridinedicarboxylate. *Inorg. Chim. Acta* **2018**, *469*, 440–446. [CrossRef]

35. Pfletscher, M.; Wölper, C.; Gutmann, J.S.; Mezger, M.; Giese, M. A modular approach towards functional supramolecular aggregates—Subtle structural differences inducing liquid crystallinity. *Chem. Commun.* **2016**, *52*, 8549–8552. [CrossRef] [PubMed]

36. Giese, M.; Krappitz, T.; Dong, R.Y.; Michal, C.A.; Hamad, W.Y.; Patrick, B.O.; MacLachlan, M.J. Tuning the photonic properties of chiral nematic mesoporous organosilica with hydrogen-bonded liquid-crystalline assemblies. *J. Mater. Chem. C* **2015**, *3*, 1537–1545. [CrossRef]

37. Pfletscher, M.; Hölscher, S.; Wölper, C.; Mezger, M.; Giese, M. Structure–Property Relationships in Hydrogen-Bonded Liquid Crystals. *Chem. Mater.* **2017**, *29*, 8462–8471. [CrossRef]

38. Kobylarczyk, J.; Pakulski, P.; Potępa, I.; Podgajny, R. Binary and Ternary Core–Shell Crystals of Polynuclear Coordination Clusters via Epitaxial Growth. *under revision*.

39. Shanmugaraju, S.; Bar, A.K.; Joshi, S.A.; Tatil, P.Y.P.; Mukherjee, P.S. Constructions of 2D-Metallamacrocycles Using Half-Sandwich Ru^{II}₂ Precursors: Synthesis, Molecular Structures, and Self-Selection for a Single Linkage Isomer. *Organometallics* **2011**, *30*, 1951–1960. [CrossRef]

40. Cho, Y.L.; Uh, H.; Chang, S.-Y.; Chang, H.-Y.; Choi, M.-G.; Shin, I.; Jeong, K.-S. A Double-Walled Hexagonal Supermolecule Assembled by Guest Binding. *J. Am. Chem. Soc.* **2001**, *123*, 1258–1259. [CrossRef]

41. Sekiya, R.; Nishikiori, S.; Ogura, K. Crystalline Inclusion Compounds Constructed through Self-Assembly of Isonicotinic Acid and Thiocyanato Coordination Bridges. *J. Am. Chem. Soc.* **2004**, *126*, 16587–16600. [CrossRef]

42. Trokowski, R.; Akine, S.; Nabeshima, T. Synthesis, characterization and molecular recognition of a bis-platinum terpyridine dimer. *Chem. Commun.* **2008**, 889–890. [CrossRef] [PubMed]

43. Shankar, K.; Kirillov, A.M.; Baruah, J.B. A modular approach for molecular recognition by zinc dipicolinate complexes. *Dalton Trans.* **2015**, *44*, 14411–14423. [CrossRef] [PubMed]

44. Blanco, V.; Abella, D.; Rama, T.; Alvarino, C.; García, M.D.; Peinador, C.; Quintela, J.M. Guest-induced stereoselective self-assembly of quinoline-containing Pd^{II} and Pt^{II} metallacycles. *RSC Adv.* **2016**, *6*, 80181–80192. [CrossRef]

45. Singh, M.P.; Baruah, J.B. Stable host–guest complexes of bis-2,6-pyridinedicarboxylate iron(III) with dihydroxybenzenes. *Polyhedron* **2017**, *138*, 103–108. [CrossRef]

46. Shankar, K.; Baruah, J.B. Inclusion of dihydroxyaromatics by a lanthanum(III) 2,6-dipicolinate complex. *Polyhedron* **2017**, *126*, 262–267. [CrossRef]

47. Bernstein, J.; Davis, R.E.; Shimoni, L.; Chang, N.-L. Patterns in Hydrogen Bonding: Functionality and Graph Set Analysis in Crystals. *Angew. Chem. Int. Ed.* **1995**, *34*, 1555–1573. [CrossRef]

48. Paul, M.; Desiraju, G.R. From a Binary to a Quaternary Cocrystal: An Unusual Supramolecular Synthon. *Angew. Chem. Int. Ed.* **2019**, *58*, 12027–12031. [CrossRef]

49. Steiner, T. The Hydrogen Bond in the Solid State. *Angew. Chem. Int. Ed.* **2002**, *41*, 48–76. [CrossRef]

50. Alvarez, S.; Alemany, P.; Casanova, D.; Cirera, J.; Llunell, M.; Avnir, D. Shape maps and polyhedral interconversion paths in transition metal chemistry. *Coord. Chem. Rev.* **2005**, *249*, 1693–1708. [CrossRef]

51. Dance, I.; Scudder, M. Supramolecular Motifs: Concerted Multiple Phenyl Embraces between Ph_4P^+ Cations Are Attractive and Ubiquitous. *Chem.-Eur. J.* **1996**, *2*, 481–486. [CrossRef]

52. Kuzniak, E.; Hooper, J.; Srebro-Hooper, M.; Kobylarczyk, J.; Dziurka, M.; Musielak, B.; Pinkowicz, D.; Raya, J.; Ferlay, S.; Podgajny, R. A concerted evolution of supramolecular interactions in a {cation; metal complex; π-acid;solvent} anion-π system. *Inorg. Chem. Front.* **2020**, *7*, 1851–1863. [CrossRef]

53. Parker, R.J.; Spiccia, L.; Batten, S.R.; Cashion, J.D.; Fallon, G.D. The Encapsulation of Ferrocyanide by Copper(II) Complexes of Tripodal Tetradentate Ligands. Novel H-Bonding Networks Incorporating Heptanuclear and Pentanuclear Heterometallic Assemblies. *Inorg. Chem.* **2001**, *40*, 4696–4704. [CrossRef] [PubMed]

54. Bencini, A.; Bianchi, A.; Garcia-Espana, E.; Giusti, M.; Mangani, S.; Micheloni, M.; Orioli, P.; Paoletti, P. Anion coordination chemistry. 2. Electrochemical, thermodynamic, and structural studies on supercomplex formation between large polyammonium cycloalkanes and the two complex anions hexacyanoferrate(II) and hexacyanocobaltate(III). *Inorg. Chem.* **1987**, *26*, 3902–3907. [CrossRef]

55. Brorson, M.; Galsbøl, F.; Simonsen, K.; Skov, L.K.; Søtofte, I. Preparation and Characterization of cis- and trans-$[Ir(tn)_2Cl_2]CF_3SO_3$ and of $[Ir(tn)_3]Cl_3$ (tn=propane-1,3-diamine). *Acta Chem. Scand.* **1998**, *52*, 1017–1023. [CrossRef]

56. Kou, H.Z.; Jiang, Y.-B.; Zhou, B.C.; Wang, R.J. Cyano-Bridged 2D $Cu^{II}-Cr^{III}$ Coordination Polymers: Structural Evidence for Formation of a Polymeric Macrocyclic Metallic Compound. *Inorg. Chem.* **2004**, *43*, 3271–3276. [CrossRef]

57. Cvrtila, I.; Stilinović, V. New Tricks by Old Anions: Hydrogen Bonded Hexacyanoferrous Anionic Networks. *Cryst. Growth Des.* **2017**, *17*, 6793–6800. [CrossRef]

58. Alborés, P.; Slep, L.D.; Weyhermüller, T.; Rentschler, E.; Baraldo, L.M. Exchange coupling across the cyanide bridge: Structural and DFT interpretation of the magnetic properties of a binuclear chromium(III) complex. *Dalton Trans.* **2006**, 948–954. [CrossRef]

59. Graham, M.J.; Zadrozny, J.M.; Shiddiq, M.; Anderson, J.S.; Fataftah, M.S.; Hill, S.; Freedman, D.E. Influence of Electronic Spin and Spin–Orbit Coupling on Decoherence in Mononuclear Transition Metal Complexes. *J. Am. Chem. Soc.* **2014**, *136*, 7623–7626. [CrossRef]

60. Spackman, M.A.; Jayatilaka, D. Hirshfeld surface analysis. *CrystEngComm* **2009**, *11*, 19–32. [CrossRef]

61. Spackman, M.A.; McKinnon, J.J. Fingerprinting intermolecular interactions in molecular crystals. *CrystEngComm* **2002**, *4*, 378–392. [CrossRef]

62. Spackman, P.R.; Turner, M.J.; McKinnon, J.J.; Wolff, S.K.; Grimwood, D.J.; Jayatilaka, D.; Spackman, M.A. CrystalExplorer: A program for Hirshfeld surface analysis, visualization and quantitative analysis of molecular crystals. *J. Appl. Crystallogr.* **2021**, *54*, 1006–1011. [CrossRef] [PubMed]

63. Caldeweyher, E.; Ehlert, S.; Hansen, A.; Neugebauer, H.; Spicher, S.; Bannwarth, C.; Grimme, S. A generally applicable atomic-charge dependent London dispersion correction. *J. Chem. Phys.* **2019**, *150*, 154122. [CrossRef] [PubMed]

64. Coupar, P.I.; Ferguson, G.; Glidewell, C. Hydrogen-Bonded Chains in 4,4′-Dihydroxybenzophenone-4,4′-Bipyridyl (1/1) and Chains of Rings in 1,3,5-Trihydroxybenzene-4,4′-Bipyridyl (2/3). *Acta Cryst.* **1996**, *C52*, 2524–2528. [CrossRef]

65. Goerigk, L.; Mehta, N. Trip to the Density Functional Theory Zoo: Warnings and Recommendations for the User. *Aust. J. Chem.* **2019**, *72*, 563–573. [CrossRef]

66. Mitoraj, M.P.; Michalak, A.; Ziegler, T. A Combined Charge and Energy Decomposition Scheme for Bond Analysis. *J. Chem. Theory Comput.* **2009**, *5*, 962–975. [CrossRef]

67. van der Lubbe, S.C.C.; Guerra, C.F. The Nature of Hydrogen Bonds: A Delineation of the Role of Different Energy Components on Hydrogen Bond Strengths and Lengths. *Chem.-Asian J.* **2019**, *14*, 2760–2769.

68. Perruchas, S.; Boubekeur, K.; Molinié, P. Radical cation salts of $TTF(CH_2OH)_4$ with cyanide anions: Synthesis, crystal structure and magnetic properties of $[TTF(CH_2OH)_4][TCNQF_4]$ and $[TTF(CH_2OH)_4]_3[18$-crown-6 ⊂ $K][M(CN)_6]$·DMF (M = Fe, Co). *Polyhedron* **2005**, *24*, 1555–1564. [CrossRef]

69. Hanuza, J.; Strek, W.; Hermanowicz, K.; Jezowska-Trzebiatowska, B.; Trabjerg, I. Spectroscopic behaviour of $Cr(CN)_6^{3-}$ ion isolated in KCl host. *J. Mol. Struct.* **1986**, *144*, 141–153. [CrossRef]

70. Jain, S.C.; Warrier, A.V.R.; Sehgal, H.K. Vibrational and electronic properties of $Co(CN)_6^{3-}$ doped in alkali halides. *J. Phys. C Sol. St. Phys.* **1972**, *5*, 1511–1518. [CrossRef]

71. Ross, M.; Andersen, A.; Fox, Z.W.; Zhang, Y.; Hong, K.; Lee, J.-H.; Cordones, A.; March, A.M.; Doumy, G.; Southworth, S.H.; et al. Comprehensive Experimental and Computational Spectroscopic Study of Hexacyanoferrate Complexes in Water: From Infrared to X-ray Wavelengths. *J. Phys. Chem. B* **2018**, *122*, 5075–5086. [CrossRef]

72. Kuzniak, E.; Pinkowicz, D.; Hooper, J.; Srebro-Hooper, M.; Hetmańczyk, Ł.; Podgajny, R. Molecular Deformation, Charge Flow, and Spongelike Behavior in Anion–π $\{[M(CN)_4]^{2-};[HAT(CN)_6]\}_\infty$ (M=Ni, Pd, Pt) Supramolecular Stacks. *Chem. Eur. J.* **2018**, *24*, 16302–16314. [CrossRef] [PubMed]

73. Martinez-Garcia, R.; Knobel, M.; Reguera, E. Modification of the magnetic properties in molecular magnets based on Prussian blue analogues through adsorbed species. *J. Phys. Condens. Matter* **2006**, *18*, 11243–11254. [CrossRef]

74. Hendrickx, M.F.A.; Mironov, V.S.; Chibotaru, L.F.; Ceulemans, A. An *Ab Initio* Study of the Ligand Field and Charge-Transfer Transitions of $Cr(CN)_6^{3-}$ and $Mo(CN)_6^{3-}$. *J. Am. Chem. Soc.* **2003**, *125*, 3694–3695. [CrossRef] [PubMed]

75. Hanuza, J.; Strek, W.; Hermanowicz, K.; Jezowska-Trzebiatowska, B.; Trabjerg, I. Spectroscopic properties of $Cr(CN)_6^{3-}$ doped in a KBr crystal. *Chem. Phys.* **1984**, *86*, 137–145. [CrossRef]

76. Mitsuru, S.; Hirohiko, A.; Hideo, Y. The DV-Xα MO Study of the Electronic Structures of $[M(CN)_6]^{3-}$ (M = Cr, Mn, Fe, and Co) and $[Fe(CN)_6]^{4-}$. *Bull. Chem. Soc. Jap.* **1981**, *54*, 2898–2903.

77. Alexander, J.J.; Gray, H.B. Electronic structures of hexacyanometalate complexes. *J. Am. Chem. Soc.* **1968**, *90*, 4260–4271. [CrossRef]

78. Sreekantan, S.; Lalithambika, N.; Atak, K.; Seidel, R.; Neubauer, A.; Brandenburg, T.; Xiao, J.; Winter, B.; Aziz, E.F. Chemical bonding in aqueous hexacyano cobaltate from photon- and electron-detection perspectives. *Sci. Rep.* **2017**, *7*, 40811.

79. Sano, M.; Hatano, Y.; Kashiwagi, H.; Yamatera, H. An Ab Initio Calculations of the Electronic Structure of the $[Co(CN)_6]^{3-}$ Ion. *Bull. Chem. Soc. Jap.* **1981**, *54*, 1523–1530. [CrossRef]

80. Hahn, A.W.; Van Kuiken, B.E.; Chilkuri, V.G.; Levin, N.; Bill, E.; Weyhermüller, T.; Nicolaou, A.; Miyawaki, J.; Harada, Y.; DeBeer, S. Probing the Valence Electronic Structure of Low-Spin Ferrous and Ferric Complexes Using 2p3d Resonant Inelastic X-ray Scattering (RIXS). *Inorg. Chem.* **2018**, *57*, 9515–9530. [CrossRef]

81. Ojeda, J.; Arrell, C.A.; Longetti, L.; Chergui, M.; Helbing, J. Charge-transfer and impulsive electronic-to-vibrational energy conversion in ferricyanide: Ultrafast photoelectron and transient infrared studies. *Phys. Chem. Chem. Phys.* **2017**, *19*, 17052–17062. [CrossRef]

82. Yu, P.; Yang, F.; Zhao, J.; Wang, J. Hydration Dynamics of Cyanoferrate Anions Examined by Ultrafast Infrared Spectroscopy. *J. Phys. Chem. B* **2014**, *118*, 3104–3114. [CrossRef]

83. Zhang, W.; Ji, M.; Sun, Z.; Gaffney, K.J. Dynamics of Solvent-Mediated Electron Localization in Electronically Excited Hexacyanoferrate(III). *J. Am. Chem. Soc.* **2012**, *134*, 2581–2588. [CrossRef] [PubMed]

84. Chorazy, S.; Sieklucka, B.; Ohkoshi, S. Near-Infrared Photoluminescence in Hexacyanido-Bridged Nd–Cr Layered Ferromagnet. *Cryst. Growth Des.* **2016**, *16*, 4918–4925. [CrossRef]

85. Kitzmann, W.R.; Moll, J.; Heinze, K. Spin-flip luminescence. *Photochem. Photobiol. Sci.* **2022**. [CrossRef] [PubMed]

86. Yang, D.; Liang, Y.; Ma, P.; Li, S.; Wang, J.; Niu, J. Self assembly of carboxylate/alcoholate functionalized ring-shape phosphomolybdates. *CrystEngComm* **2014**, *16*, 8041–8046. [CrossRef]

87. Wang, Y.-J.; Liu, J.-L.; Yang, H.-M.; Jia, A.-Q.; Zhang, Q.-F. Inclusion of ferrocene within the deepened cavities formed from the hydrogen bonding self-assembly of calix[4]resorcinarenes with bis-pyridines. *J. Incl. Phenom. Macro.* **2016**, *85*, 105–110. [CrossRef]

88. Papaefstathiou, G.S.; Darrow, B.G.; MacGillivray, L.R. Crystal and molecular structure of $[Cu2(3,5-dihydroxybenzoate)_4$ (acetonitrile)$_2]\cdot 8H_2O$. *J. Chem. Crystallogr.* **2002**, *32*, 191–195. [CrossRef]

89. Feng, L.; Chen, Z.; Zeller, M.; Luck, R.L. Dicopper moieties stabilized by Fréchet-type dendrons: Syntheses and structural characterizations. *Polyhedron* **2014**, *80*, 206–215. [CrossRef]

90. Chaumont, C.; Mobian, P.; Kyritsakas, N.; Henry, M. Synthesis, topology and energy analysis of crystalline resorcinol-based oligophenylene molecules with various symmetries. *CrystEngComm* **2013**, *15*, 6845–6862. [CrossRef]

91. Dan, M.; Cheetham, A.K.; Rao, C.N.R. Diverse Structures and Dimensionalities in Hybrid Frameworks of Strontium and Lanthanum with Isomeric Dihydroxybenzoates. *Inorg. Chem.* **2006**, *45*, 8227–8238.

92. Liwporncharoenvong, T.; Luck, R.L. Quadruply Bonded Dimolybdenum Atoms Surrounded by Dendrons: Preparation, Characterization, and Electrochemistry. *J. Am. Chem. Soc.* **2001**, *123*, 3615–3616. [CrossRef] [PubMed]

93. Bhyrappa, P.; Wilson, S.R.; Suslick, K.S. View Author Information Hydrogen-Bonded Porphyrinic Solids: Supramolecular Networks of Octahydroxy Porphyrins. *J. Am. Chem. Soc.* **1997**, *119*, 8492–8502. [CrossRef]

94. Sheldrick, G. A short history of SHELX. *Acta Crystallogr. Sect. A Found. Crystallogr.* **2008**, *64*, 112–122. [CrossRef] [PubMed]

95. Sheldrick, G. Crystal structure refinement with SHELXL. *Acta Crystallogr. Sect. C Struct. Chem.* **2015**, *71*, 3–8. [CrossRef]

96. Dolomanov, O.V.; Bourhis, L.J.; Gildea, R.J.; Howard, J.A.K.; Puschmann, H. *OLEX2*: A complete structure solution, refinement and analysis program. *J. Appl. Crystallogr.* **2009**, *42*, 339–341. [CrossRef]

97. Macrae, C.F.; Sovago, I.; Cottrell, S.J.; Galek, P.T.A.; McCabe, P.; Pidcock, E.; Platings, M.; Shields, G.P.; Stevens, J.S.; Towler, M.; et al. Mercury 4.0: From visualization to analysis, design and prediction. *J. Appl. Crystallogr.* **2020**, *53*, 226–235. [CrossRef]

98. te Velde, G.; Bickelhaupt, F.M.; Baerends, E.J.; Fonseca Guerra, C.; van Gisbergen, S.J.A.; Snijders, J.G.; Ziegler, T. Chemistry with ADF. *J. Comput. Chem.* **2001**, *22*, 931–967. [CrossRef]

99. ADF 2019.304, SCM, Theoretical Chemistry, Vrije Universiteit, Amsterdam, The Netherlands. Available online: https://www.scm.com (accessed on 21 April 2022).

100. Becke, A.D. Density-Functional Exchange-Energy Approximation with Correct Asymptotic Behavior. *Phys. Rev. A* **1988**, *38*, 3098–3100. [CrossRef]

101. Lee, C.; Yang, W.; Parr, R.G. Development of the Colle-Salvetti Correlation-Energy Formula into a Functional of the Electron Density. *Phys. Rev. B* **1988**, *37*, 785–789. [CrossRef]

102. Becke, A.D. Density-Functional Thermochemistry. III. The Role of Exact Exchange. *J. Chem. Phys.* **1993**, *98*, 5648–5652. [CrossRef]

103. Stephens, P.J.; Devlin, F.J.; Chabalowski, C.F.; Frisch, M.J. Ab Initio Calculation of Vibrational Absorption and Circular Dichroism Spectra Using Density Functional Force Fields. *J. Phys. Chem.* **1994**, *98*, 11623–11627. [CrossRef]

104. Santra, G.; Sylvetsky, N.; Martin, J.M.L. Minimally Empirical Double-Hybrid Functionals Trained against the GMTKN55 Database: RevDSD-PBEP86-D4, RevDOD-PBE-D4, and DOD-SCAN-D4. *J. Phys. Chem. A* **2019**, *123*, 5129–5143. [CrossRef] [PubMed]

105. Klamt, A.; Schüürmann, G. COSMO: A New Approach to Dielectric Screening in Solvents with Explicit Expressions for the Screening Energy and Its Gradient. *J. Chem. Soc. Perkin Trans.* **1993**, *2*, 799–805. [CrossRef]

106. Klamt, A. Conductor-like Screening Model for Real Solvents: A New Approach to the Quantitative Calculation of Solvation Phenomena. *J. Phys. Chem.* **1995**, *99*, 2224–2235. [CrossRef]

107. van Lenthe, E.; Baerends, E.J.; Snijders, J.G. Relativistic Regular Two-Component Hamiltonians. *J. Chem. Phys.* **1993**, *99*, 4597–4610. [CrossRef]

108. van Lenthe, E.; Baerends, E.J.; Snijders, J.G. Relativistic Total Energy Using Regular Approximations. *J. Chem. Phys.* **1994**, *101*, 9783–9792. [CrossRef]

109. Mitoraj, M.; Michalak, A. Natural Orbitals for Chemical Valence as Descriptors of Chemical Bonding in Transition Metal Complexes. *J. Mol. Model.* **2007**, *13*, 347–355. [CrossRef]